Session PR-4

Packaging Reliability(4)

Straightening of Warped Products Assisted by Near-Infrared Radiation
Kimitoshi SATO, Kaichi HAYASHI, Yasuo KUROSAKI, The University of Electro-Communications, Japan
Takushi SAITO, Tokyo Institute of Technology

Singular Stress Analysis in a Viscoelastic Thin Layer Bonded to an Elastic Substrate using Realistic Relaxation Function
Sang Soon LEE, Korea University of Technology and Education, Korea

The Study of Failure Mechanism and Chip Warpage for DCA Components
C. Y. HUANG, J. R. LIN, HuaFan University, Taiwan
K. SRIHARI, State University of New York at Binghamton, USA

Analysis of Three Dimensional Crack Corners via Conservation Integral
Yongwoo LEE, Seyoung IM, Korea Advanced Institute of Sciene and Technology, Korea
Dong-Won JUNG, Cheju National University, Korea

Straightening of Warped Products Assisted by Near-Infrared Radiation

Kimitoshi Sato[*1], Kaichi Hayashi[*1], Takushi Saito[*2] and Yasuo Kurosaki[*1]
[*1]The University of Electro-Communications
1-5-1 Chofugaoka, Chofu, Tokyo 182-8585, Japan
[*2] Tokyo Institute of Technology
2-12-1 Ookayama, Meguro-ku, Tokyo 152-8552, Japan
ksato@mce.uec.ac.jp, +81-424-43-5417

Abstract

A reform method of the warped products by utilizing press molding assisted by a near-infrared radiative heating right after an injection molding process is proposed and investigated its feasibility in this paper. Since the temperature of irradiated component rises due to absorption of radiation, the plasticity of polymer consequently increases, and then the flat component is produced in the proposed process. First the effect of heating by near-infrared radiation on the reduction of warpage of a LCP product has been studied experimentally. Then the temperature distribution within the product and molds was obtained by numerical calculation in order to estimate the validity of the proposing method. It was considered that the influence of the thermal conductivity of the mold system and convective heat transfer are dominant for the processing cycle time.

Introduction

Plastics are currently used in many advanced electronic components. They are commonly produced by injection molding with keeping high productivity. During the injection molding process, molten polymer is injected with a high flow rate into a cold mold cavity maintained below the glass transition temperature of polymer, then cooled from its surface in contact with the cold mold wall, and a thin solidified layer is formed. Because of the high viscosity in this layer, injection molded polymer products inherently suffer some problems such as shape deformation and residual stress. Even though a product stands up to the test of the dimensional accuracy after the injection molding process but contains the “invisible” process-induced residual stress, the problem arises in the after; shrinking and warpage due to the release of residual stress may appear after a heating opportunity like the reflow soldering (see Fig.1). The deformation of the parts causes a poor contacting among the components in the mounting process.

Fundamentally, the generation of the solidification layer is suppressed by controlling the heat transfer between the mold wall and the molten polymer. Jansen *et al* [1], Kim et al [2] and Yao et al [3] utilized a thin electric heater pasted on the mold walls with an insulation layer to prevent the heat loss from the molten polymer during the filling stage. These methods show the effect on the improvement of the products; however, they hold the difficulty in the reduction of the cycle time due to the existence of the insulation layer as a thermal resistance and the thermal expansion-mismatching problem, which attacks the layered system. These problems result to deprive the advantage of easy handling of injection molding. Therefore a new processing method, which is simple and efficient, is necessary for the precise products.

In order to overcome such problems, the authors propose a processing method having two stages such as injection molding and straightening-treatment using a near-infrared radiation. In this paper, the influence of the heat generation due to the radiative transfer within the liquid crystal polymer components, the heat conduction within the mold system and the convective heat transfer during the cooling on the straightening of the warpage has been studied experimentally. Also the temperature distributions within the product and the molds were obtained by numerical calculation in order to estimate the validity of proposing method for the processing with rapid heating and cooling.

Experimental

The concept of the propositional process is shown in Fig.1. A warped component or a one having latent warpage produced in a conventional injection molding process is inserted into a mold cavity to be heated and pressed. Then the softened component after heating is corrected in the right shape within the solid mold. In order to heat the component, a near-infrared radiation is applied in this process. Thermoplastic materials absorb certain irradiated energy and generate heat. On the other hand, glass materials are well transparent to infrared radiation. Therefore using an opaque glass window transparent

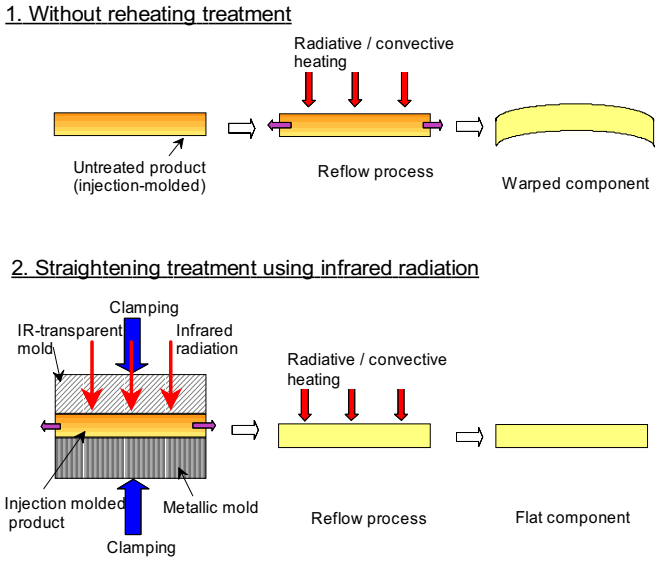

Fig. 1 Concept of straightening treatment with near-infrared radiative heating

to infrared radiation as a mold, a near-infrared beam is irradiated to the plastic through it. Since the temperature of the component rises due to absorption of radiation, the fluidity of polymer consequently increases.

The authors have investigated a process to improve both the optical quality and replication of the plastic components by applying infrared radiation on the moving polymer melt (polystyrene) injected in the mold cavity through the IR-transparent window provided on the mold wall [4,5,6]. In those studies a zinc selenide (ZnSe) window had to be adopted to the mold system to guide a CO_2 laser beam [10.6μm] into the cavity. In this study, liquid crystal polymer (LCP) has high absorbency (low transparency) to near infrared radiation as shown in Fig.2, therefore, PYREX glass, prevailing glass material transparent to near infrared radiation, is able to be applied.

In this press molding process for the straightening of the products, there are not any heating elements within the mold system: it is able to be in a low temperature, and therefore cooling is rapidly accomplished or it doesn't need a complicated cooling bus system within the molds.

LCP (XYDER-MG350, Nippon Petrochemicals Co.) was used as a molding material in this study. Figure 3 shows the schematic representation of the product geometry.

Figure 4 shows a schematic diagram of the experimental setup. The thermal properties of the materials used in the experiment are listed on Table 1. A workpiece molded in the preliminary process by injection machine is inserted into the cavity, and is covered with an infrared-transparent PYREX plates under pressure of 0.4MPa; then, the near-infrared radiation of infrared lamp (GA298, Thermo-Rikoh Co.) is applied to the inserted workpiece for a few minutes duration until the temperature of the inserted workpiece rises over 523K (the deflection temperature under load) up to 603K. After it reaches the set temperature, the mold system is cooled until it drops to 348K. Finally the workpiece is heated in an oven at 493K for ten seconds as reheating and then it is cooled by air at room temperature. The vertical deviation of the dimension of workpieces was measured after each heating/cooling stage using a laser scan micrometer.

Result and Discussion

The mold system was set at 323K as initial temperature. All the straightening experiments were carried out under the condition of ambient temperature of 300K and the irradiation intensity of 0.18 W/mm^2 in this study.

The heating curve at the surface of the workpiece is shown Fig.5. It took 170s to raise the temperature of the workpiece up to 603K.

Figure 6 shows the vertical deviation of the dimension of workpiece, which is just injection-molded before reheating. The warpage isn't significant in this stage as shown in the figure.

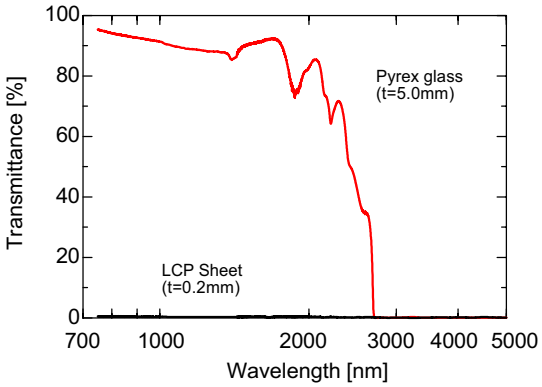

Fig. 2 Trancmittance of a LCP sheet and a glass mold

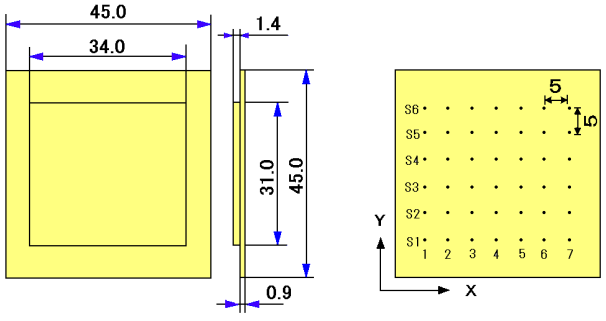

Fig. 3 Shape and size of workpiece; points of measurement of deviation

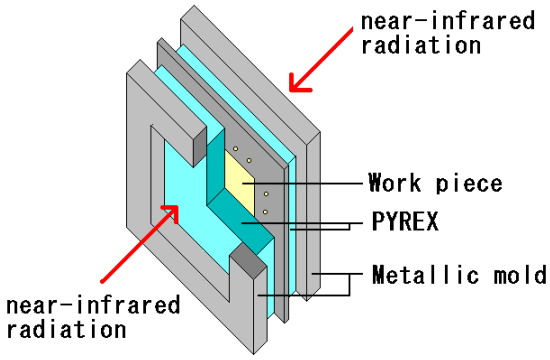

Fig.4 Experimental set up

Table 1 Thermal properties of LCP and glass materials

	LCP	PYREX 7740	Quartz crystal
Density [kg/m^3]	2230	2220	2648
Specific heat [J/kgK]	1340	890	790
Thermal conductivity [W/mK]	0.36	1.24	10.7
Absorption coefficient [m^{-1}] at 1000 [nm]	11886 (0.2mm)	-	-

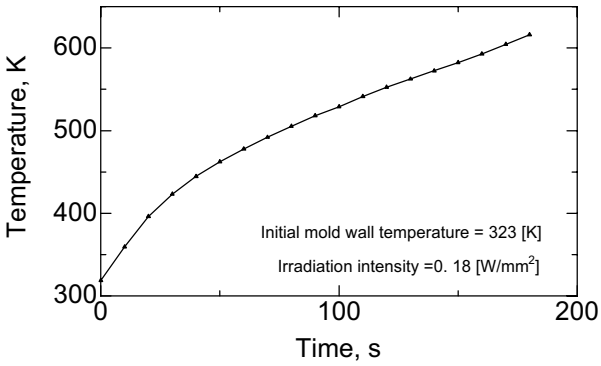

Fig.5 Heating curve (experimental)

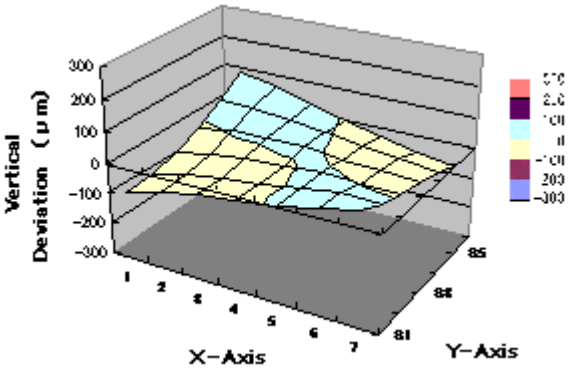

Fig. 6 Deviation of an injection molded workpiece

Then the injection-molded workpiece was heated and cooled without the mold. The vertical deviation of the dimension of the workpiece after reheating is shown in Fig.7. The maximum vertical deviation of the dimension of this workpiece reached ±200μm and this product was regarded as defective one.

In order to reduce the amount of warpage of workpieces, the injection-molded workpieces were treated with the radiative-heating straightening (up to T_{wp}=523K). Then they were also processed in the reheating stage in the oven. The treated workpiece appeared to be straitened before reheating, however, it warped again after reheating. Figure 8 shows the vertical deviation of the dimension of workpiece. The warpage was slightly decreased from ±200μm to ±150μm. The condition of the polymer used in this study at T_{wp}=523K is suppoted to be the deflection tmperature under load but not enough to be fully released residual stress.

The workpiece was heated up to the temperature of 603K, which is close to melt temperature of the polymer used. The vertical deviation of the dimension of workpiece after reheating subsequent to the radiative-heating straightening (up to T_{wp}=603) is shown in Fig.9. It was achieved that the reduction of warpage: the deviation was remitted within +100μm.

To improve the flatness of injection-molded products by a secondary process, the workpiece, especially for LCP, must be heated up to high temperature near its melting point within the molds, therefore, the control of heating and cooling is very important. The cycle time of tested process in this study is

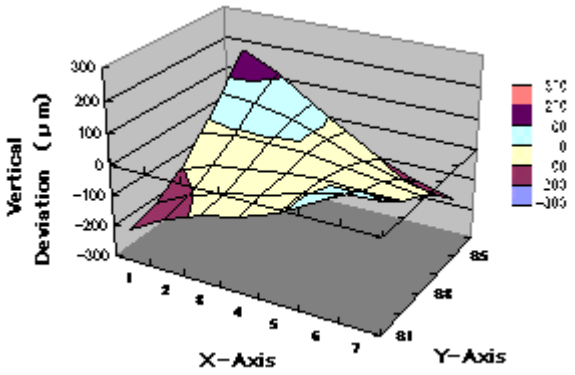

Fig.7 Deviation of a workpiece after reheating

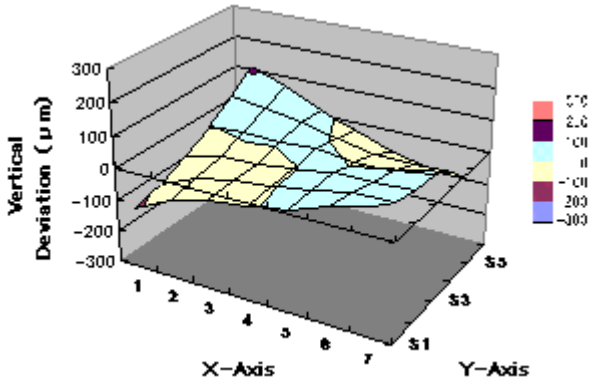

Fig.8 Deviation of a workpiece after the treatment with infrared-radiation (heating up to 523K)

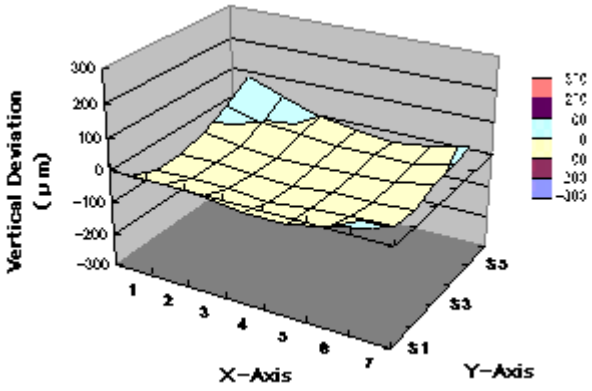

Fig.9 Deviation of a work piece after the treatment with infrared-radiation (heating up to 603K)

seemed to be somewhat long (heating of 170s and cooling of 600s). It is necessary to consider the effect of the condition of irradiation, material properties of mold and heat transfer to the ambient air in order to improve the efficiency of the process.

Numerical Simulation

The temperature distributions in the mold system were numerically estimated to assess the temperature rise and the rapid cooling of the polymeric workpiece in the proposed process. The heat transfer in this process adopted in our experiment was assumed as one-dimensional unsteady heat

conduction in a composite slab consisting of three layers: (a) glass mold / (b) polymeric workpiece / (c) glass mold, as shown in Fig. 10. Contact thermal resistance was discounted in this simulation.

Energy equation within each glass mold is expressed as follows:

$$\rho_{gm} c_{gm} \frac{\partial T}{\partial t} = k_{gm} \frac{\partial^2 T}{\partial x^2}$$

in a<x<0 and 1<x<b, for t>0 (1)

where ρ, c and k are the density, heat capacity and thermal conductivity of glass mold, respectively, T is the temperature, x is the cordinate and t is time. As the glass molds, two kinds of material: PYREX 7740 and quartz crystal are considered in this numerical simulation.

In addition, energy equation in the polymeric workpiece has a radiation term and is expressed as follows:

$$\rho_{pw} c_{pw} \frac{\partial T}{\partial t} = k_{pw} \frac{\partial^2 T}{\partial x^2} - \frac{\partial q_r}{\partial x}$$

in -1<x<1, for t>0 (2)

where q_r is the heat generation due to radiation absorption within the polymeric workpiece:

$$q_r = I_0 \exp(-\beta_{pw} x) \quad (3)$$

The initial condition of this system is a constant temperature T_0. It is assumed that the mold system dissipates heat its outer surface by convection with a heat transfer coefficient h into an ambient at room temperature T_{∞}, therfore;

$$T = T_0 \qquad \text{in } -11 \le x \le 11, \text{ for } t=0$$

$$k_{gm} \frac{\partial T}{\partial x} + hT = hT_{\infty} \qquad \text{at } x=-11 \text{and } 11, \text{ for } t>0$$

$$k_{gm} \frac{\partial T}{\partial x} = k_{pw} \frac{\partial T}{\partial x} \qquad \text{at } x=0 \text{ and } 1, \text{ for } t>0$$

The governing equations were solved with a control volume finite difference approach. The thermal properties of the materials for the present simulation are also listed on Table 1. The processing conditions of this numerical simulation are cited on Table 2.

Figure 11 shows the temperature distribution within the mold system after the irradiation. The notable feature is that the maximum temperature emerges in the polymeric workpiece apart from the surface. The reason is that the IR transparent window contact with the polymeric workpiece works as a heat sink, which diffuses thermal energy from the polymeric workpiece, and consequently drops down the surface temperature. The heat conductivity of polymer is so small that the heat due to radiation absorption in the interior

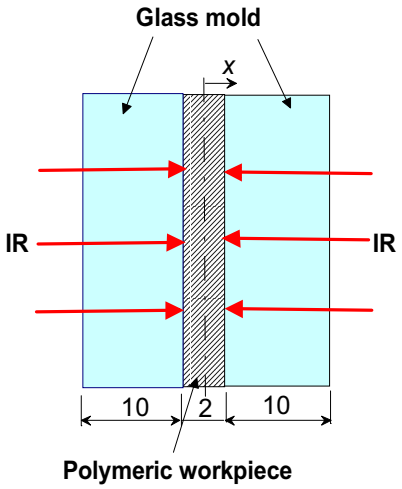

Fig.10 Numerical analysis model

Table 2 Processing conditions used for the present numerical simulation

I_0	[W/mm^2]	0.18
T_8	[K]	300
T_0	[K]	323

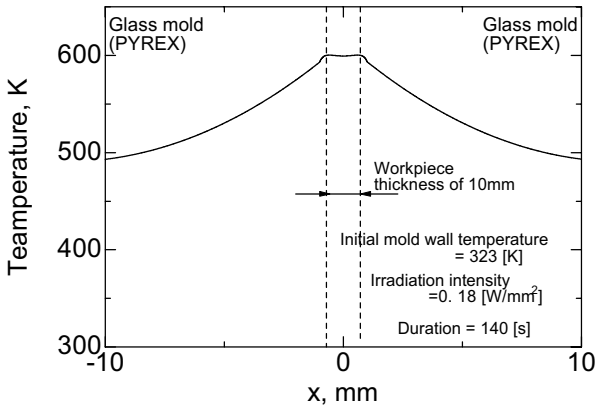

Fig. 11 Temperature distribution

domain is not affected at all; therefore, higher temperature remains inside unaffected. In the case of heating by the electrical heater embedded within the mold, on the contrary, the maximum temperature emerges at the surface. Such a high surface temperature is afraid to give unfavorable effects on the polymer surface quality.

In order to investigate the effect of the properties of the material used as the glass molds and heat transfer coefficient at the surface of the mold system on the reduction of processing cycle time, the cooling curve at the surface of the workpiece was also simulated. Two levels of glass mold

thickness; 5 and 10 mm, and three levels of heat transfer coefficient; 15, 45, 75 W/m^{2}K were examined. Further, to evaluate the effect of thermal conductivity of glass mold, the cooling curve in the case using a quartz crystal, which shows higher heat conductivity than PYREX was also calculated.

Figure 12and 13 show the heating and cooling curves at a PYREX glass mold thickness of 10 mm and 5 mm, respectively. The thinner glass mold is used, the faster cooling rate is available. It is considerable that it doesn't take time so much to dissipate heat from a mold having small heat capacity.

Figure 14 shows the heating and cooling curves at the quartz crystal glass mold thickness of 5 mm. Unfortunately, the cooling time is lengthened when the thermal conductivity of the glass mold is higher than that of PYREX. Since the effect as a heat sink greatly comes, most of heat transfer to the glass during the heating stage, then the temperature of the glass mold is raised so much in order to heat the workpiece properly. Therefore the cooling ability isn't improved even in the condition of higher heat coefficient. From a thermal point of view, the consideration of the heat loss from the workpiece to the mold during the heating stage is important, and therefore the material having high thermal conductivity is unsuitable to this process.

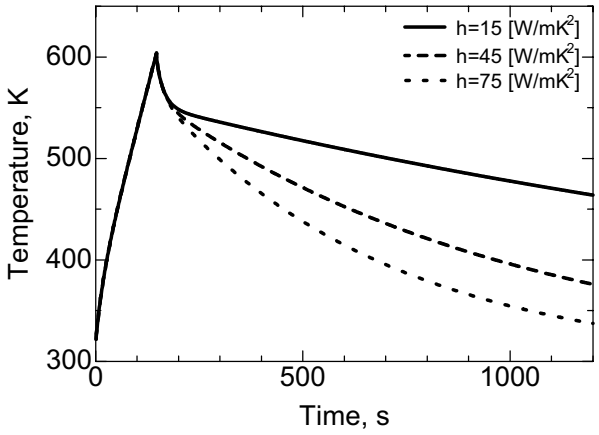

Fig.12 Influence of heat transfer coefficient at the outer surface of glass mold on cooling curve (10mm thick PYREX glass mold)

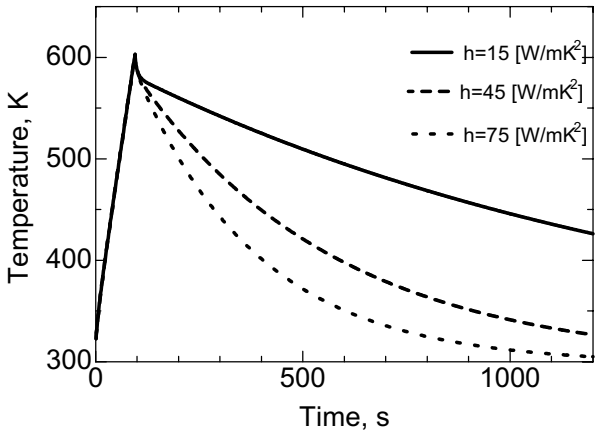

Fig.13 Influence of heat transfer coefficient at the outer surface of glass mold on cooling curve (5mm thick PYREX glass mold)

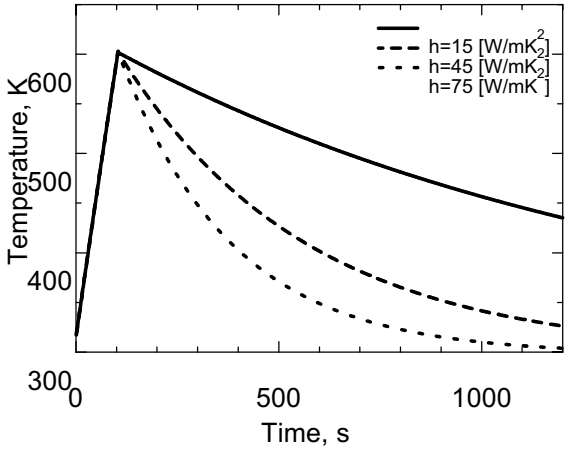

Fig.14 Cooling curve (5mm thick quartz crystal mold)

Conclusions

An efficient heating and cooling mold system for the straightening of the warped products has been studied experimentally and numerically. LCP workpiece had to be heated up to high temperature near its melting point within the molds. It was confirmed that the proposing heating method had the ability of heating to satisfy the claim for the process. The temperature distributions within the product and molds were obtained by numerical calculation in order to estimate the validity of the proposing method. It was suggested that small heat capacity due to a thin mold wall, the perpendicular temperature gradient down to the outer surface of the mold due to its low thermal conductivity and heat transfer to an ambient are directly influence on the reduction of cooling time.

Nomenclatures

c	=	specific heat, J/kgK
h	=	heat transfer coefficient, W/m^{2}K
H	=	thickness, mm
I	=	irradiation intensity, W/mm^2
k	=	thermal conductivity, W/mK
q_r	=	heat generation due to the radiation absorption, W/mm^2
T	=	temperature, K
t	=	time, s
x	=	coordinate
β	=	absorption coefficient, m^{-1}
ρ	=	density, kg/m^3

Subscripts

0	=	initial
gm	=	glass mold

pw = polymeric wokpiece
8 = ambient

Acknowledgments

This work was supported in part by Japan Society for the Promotion of Science under the grant of the Venture SME-University Research Promotion Program.

References

1. Liou, M. J. and Suh, N. P., "Reducing Residual Stresses in Molded Parts", *Polymer Engineering and Science*, Vol.29,No.7, (1989), pp.441-447
2. Jansen, K.M.B. and Flaman, A.A.M., "Construction of Fast-Response Heating elements for Injection Molding Applications", *Polymer Engineering and Science*, Vol.34, No.11 (1994), pp.894-897.
3. Yao, D., Chen, M. and Kim, B., "Development of Rapid Heating and Cooling Mold Inserts Comprising a Heating layer an Insulation layer and a substrate", ANTEC2001, Dallas, TX, May 2001, pp.704-708.
4. Kurosaki, Y., Satoh, I. and Saito, T., "Precision Polymer Injection Molding Process Assisted by Infrared Radiation to Upgrade both Optical Quality and Transcribability", *Proc.ASPE Spring Topical Meeting on Precision fabrication and Replication*, Chapell Hill, NC, Apr. 1999, pp.46-49.
5. Kurosaki, Y., Satoh, I. and Saito, T., "Heat Transfer Aspect to Upgrade the Quality of Plastics", *Proc. Symposium of Energy Engineering in the 21 Century*, Hong Kong, China, Jan. 2000, pp.84-95.
6. Kurosaki, Y. and Sato, K., "A Novel Polymer Processing Assisted by Infrared Radiation to Attain a High Precision Transcription", *Proc. 15th ASPE Annual Meeting*, Scottsdale, AZ, Oct. 2000, pp.156-159.

THE STUDY OF FAILURE MECHANISM AND CHIP WARPAGE FOR DCA COMPONENTS

C.Y. Huang, Ph.D., J.R. Lin
Industrial Management Department, HuaFan University,
No.1, HuaFan Rd., Shihtin Hsiang, Taipei Hsien, 223, Taiwan, ROC
Tel: 886-2-26632102 ext 4312 Fax: 886-2-26633981
E-mail: huang107@ms17.hinet.net
K. Srihari, Ph.D.
Department of Systems Science and Industrial Engineering
State University of New York at Binghamton
Binghamton, New York, 13902-0805, USA
Tel: 607-777-4410
E-mail: srihari@binghamton.edu

Abstract

Encapsulation of Direct Chip Attach (DCA) devices helps reduce the impact of the thermal stress that results from the mismatch in the coefficient of thermal expansion (CTE) between the silicon chip and the substrate. In the encapsulated DCA assembly, the warpage of chip was observed due to the CTE mismatch between the silicon chip and the encapsulant/substrate. During the cooling stage of the curing for underfill, the encapsulant and the silicon die shrink at different rates and result in concave warpage of the chip. This scenario has been an issue which may degrade the package reliability or even assembly yield

Also, The adhesion of the encapsulant to the chip and the board coating are essential to the reliability of the package. Poor adhesion of the encapsulant to the chip's surface may cause the delamination at the encapsulant/chip interface and lead to electrical failures during operational cycles.

This paper studies the adhesion characteristics of an encapsulant to a DCA package. The quality of the encapsulation was inspected using a Scanning Acoustic Microscope (SAM). The various delamination mechanisms were then studied. Comparisons were made between samples assembled by different materials used, such as chip passivation layer, encapsulant materials and fluxes. Finally, the effect of encapsulant pre-cure and annealing on the chip warpage was explored.

Key word: DCA technology; Encapsulation; Warpage; Reliability; Thermal shock test

INTRODUCTION

DCA devices are encapsulated to relieve the stresses that could accumulate at the solder joints. The adhesion of the encapsulant to the chip and the board coating are essential to the reliability of the package. In addition to the metallurgical interconnections provided by the solder joint, encapsulation provides additional adhesion strength to maintain the interconnection between the chip and the substrate.

The warpage of the chip due to the CTE mismatch between the silicon chip and encapsulant/substrate has been a concern which may affect package reliability. The chip warpage could subsequently lead to the cracking of the die. Pre-curing and annealing are strategies to reduce the warpage by relaxing the stress.

Also, Poor adhesion of the encapsulant to the chip's surface may cause the delamination at the encapsulant/chip interface and lead to electrical failures during operational cycles. The adhesion strength at the chip/encapsulant and encapsulant/substrate interface depends on the condition of the surface the material needs to adhere to and the encapsulant's properties.

DCA PACKAGE WARPAGE

The warpage in the electronic assemblies due to the differences in the CTE between various layers of the package has been an issue which may degrade the package reliability or even assembly yield [5]. In the encapsulated (underfilled) DCA assembly, the warpage of chip was observed due to the CTE mismatch between the silicon chip and the encapsulant/substrate. During the cooling stage of the curing for underfill material at temperature near 150 ^{o}C, the encapsulant and the silicon die shrink at different rates and result in concave warpage of the chip.

Warpage observed in Package T

In this study, the chip is mounted on to a polyimide (flex) substrate which is covered with solder mask. The substrate has a copper stiffener ring to ensure the rigidity of the package. The stiffener has an opening area at its center, and the chip is placed inside this opening. The dimensions of the chip are 2" x 2". It has 1150 I/Os. The polyimide substrate has a dimension of 1.378" (35 mm) x 1.378" (35 mm) and a thickness of 17 mils. The resulting standoff height was between 2.5 to 3.5 mils; this area was subsequently underfilled. The curing of the various underfill materials was between 150 ^{o}C to 165 ^{o}C. The warpage along the diagonal was measured to be about 2 mils on the chip with a half inch on each side. A significant level of chip cracking was observed during subsequent destructive inspections.

A three beam theory based model for the calculation of warpage in FCOB assemblies was proposed in a relevant research [5]. The analysis assumes (i) only elastic behavior, i.e. ignore all load relaxation (creep effects) and (ii) a uniform temperature distribution across the assembly. The observed chip warpage (approximately) agreed with the prediction model. The three beam theory model suggested a warpage of approximately 3 mil.

Finally, the top surface of the assembly was covered by a copper heat spreader which was attached to the back side of the die and a copper stiffener. The presence of the heat

spreader tended to warp the chip in the opposite direction (positive direction). As the thickness of the heat spreader increased, the warpage decreased, became zero, and then increased with a positive curvature.

Effect Of Encapsulant Pre-cure/Annealing On The Chip Warpage

Significant chip warpage was observed due to the CTE mismatch between the silicon chip and the substrate. During cool down after encapsulant curing, the flex substrate shrinks more than the chip, causing warpage. Curing of the encapsulant at a lower temperature should result in slower cross-linking in the encapsulant, leading to a better structure of the cured underfill material. A reduction in stress is then expected within this material. Besides, during pre-cure (at 125 °C for example) the encapsulant may begin to adhere to the chip's surface. When the encapsulant is then cured at 150°C (above Tg), moderate warpage is introduced. However, this warpage is eliminated during subsequent cool-down before warpage in the opposite direction is eventually established. Pre-curing at 125 °C may thus potentially reduce room temperature warpage by up to 25%. However, the pre-cure could also change the mechanical properties of the underfill material such as its modulus, ductility, etc., because the resulting density of chains may be different. Annealing (low temperature post cure) may also cause some relaxation of the stress, and thus the warpage.

Some of the packages (Package T) were pre-cured for 0.5 hours at 125 °C. The packages then completed the vendor suggested cure profile. Some packages were finally annealed at 100 °C for 24 hours. The matrix of curing and the resulting chip warpage is shown in Table 1. Table 2 shows the effects of annealing on chip warpage. Figure 1 provides a comparison of the observed warpage with and without the pre-cure step. The reduction in chip warpage due to pre-cure was not found to be significant, considering the precision of the measuring technique. However, data suggests a systematic reduction of 10~15% in chip warpage due to the pre-cure step. The post cure annealing process exhibited a similar effect.

PACKAGE RELIABILITY ASSESSMENT

Sample Preparation

Specimens were used to assess the adhesion characteristics of an encapsulant to a DCA component. The chips have eutectic solder bumps. All the substrate was bumped to achieve the desired standoff height. Due to the absence of wet paste, a drum fluxer was used to apply the flux prior to component placement. The flux provided the tack force needed to retain the component in place. The flux also helped to promote wetting during subsequent reflow soldering. The thickness of the flux layer on the drum fluxer was between 2.0 to 2.5 mils. Three types of flux, Flux H, I, and K, were considered. The assembled packages were encapsulated using three types of underfill materials, Encapsulants E, J, and L.

Liquid to Liquid Thermal Shock Testing(LLTS)

The underfilled assemblies were subject to LLTS testing to accelerate the occurrence of failures (delamination). The conditions used in the LLTS procedure included temperatures

Table 1. The Matrix Of Curing Profiles And The Resulting Chip Warpage

Encapsulant Used	Cure	Chip Warp (mils)
E	125°C/0.5 hr + 150°C/2 hr	2.01
E	150°C/2 hr	2.25
E	150°C/2 hr	2.33
E	125°C/0.5 hr + 150°C/2 hr	2.10
B	150°C/0.5 hr	2.18
B	150°C/0.5 hr	2.19
B	125°C/0.5 hr + 150°C/0.5 hr	1.98
C	150°C/0.5 hr	2.2
C	150°C/0.5 hr	2.30
C	125°C/0.5 hr + 150°C/0.5 hr	2.00
C	125°C/0.5hr + 150°C/0.5 hr	1.89
F	125°C/0.5 hr + 165°C/1 hr	1.96
F	165°C/1 hr	2.19

Table 2. Effects of Annealing on Chip Warpage

Encapsulant Used	Original Chip Warpage (mils)	Chip Warpage After Annealing 24hrs @100°C
E	2.21	2.11
B	2.19	2.19
C	2.32	2.29
F	2.15	1.99

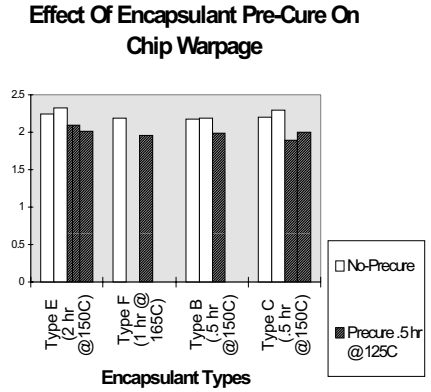

Figure 1. Chip Site Warpage With And Without Pre-Cure

of -55 °C and 125 °C with five minutes of dwell time at these temperatures. After the specimens were withdrawn from the hot tank, a wait time of 10 seconds elapsed before the specimens were transported to the cold tank. However, a wait time of a minute and fifty seconds elapsed after the specimens were withdrawn from the cold tank before the specimens were transported to the hot tank.

The Location of Delamination

The maximum stress during thermal cycling is expected to be at the corner of the package. However, only three out of sixty samples had delamination initiated from the corner of the package (Figure 2a). For the majority of the samples, delamination began at the area around the solder joints (Figure 2b). This can be explained by the following scenario. When the drum fluxer was used during assembly, the flux residues were preferentially located around the solder joint area. Flux usually does not, or is not designed to, have good adhesion to the relevant surfaces (the substrate and the passivation of the package).

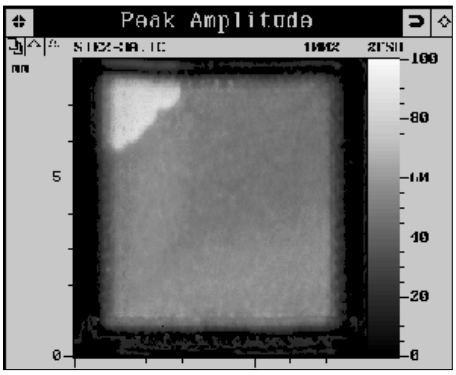

a. Delamination Initiated from a Chip Corner

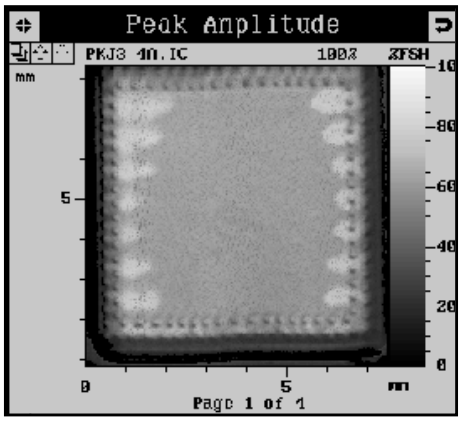

b. Delamination Initiated from the Area Around the Solder Joints

Figure 2. SAM Images Showing that the Delamination Began from Different Locations

A model experiment that was conducted helped to draw some inferences on the influence of flux residues on delamination. This model experiment consisted of the following steps. First, a board was bumped using stencil printing. The solder deposits on this board were then reflowed. The solder bumps were then coined to flatten them (the bumps). The height of the solder bumps after coining was approximately 3 mils. A wafer was placed on these coined sites. The size of the wafer was larger than the chip that would have otherwise been placed on the coined solder bump sites. Encapsulant was then dispensed along the edges. These packages were then over cured (the cure time was longer than the vendor suggested time).

In this model experiment, the initiation of delamination was observed around the solder joint area even if there was a significant distance between the periphery of the solder joint array and the edge of the package. This reinforced the conjecture that delamination would be initiated at the locations at which flux residues were present instead of being initiated at specific distances from the edge of the chip.

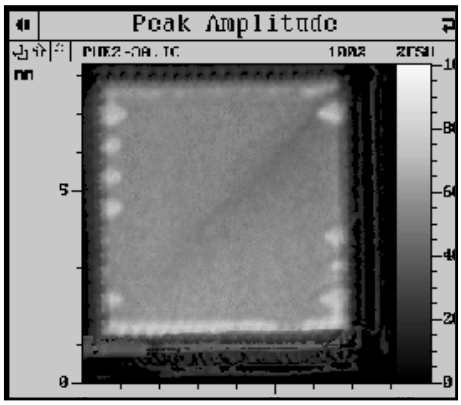

a. A Sample After 500 Cycles of LLTS

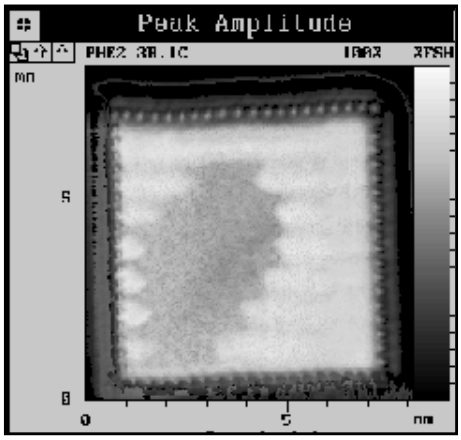

b. A Sample After 1000 Cycles of LLTS

Figure 3. SAM Images Showing that the Delamination began from the Inner Side of the Chip and Extended Inward

In this study, delamination was found to be preferentially initiated from the inner side of the solder joints with respect to the chip. It always extended inward towards the center of

the chip. Figures 3a and 3b are the SAM images of a sample after 500 and 1000 cycles of thermal shock. These samples have a polyimide passivation layer, and were assembled using Flux H and later encapsulated using Encapsulant E. The delamination that was seen extended inward and the encapsulant fillets around the four edges were still flawless. All the I/Os remained good on this sample after 1000 cycles. This observation made sense from a mechanical point of view. Solder joints are not immediately stressed and can still survive as long as the underfill material is present at the edges of the chip and it (the underfill) can couple the package with the board. The shape of the encapsulant's fillet is important. Figure 4 is a cross-section of a sample which shows delamination near the solder bump due to the presence of flux residue. In this case also, delamination appeared only on the inner side of the joint.

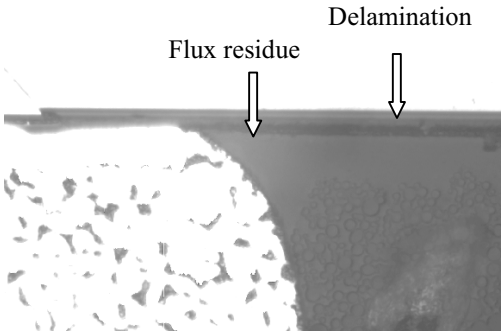

Figure 4. A Cross-Section Showing the Delamination Near the Solder Bump Due to the Presence of Flux Residue

The samples used in the model experiment (discussed above) exhibited a smaller degree of delamination when compared to the samples used in this study. The ranking of the degree of delamination for different underfill materials was however consistent. While the solder joint layout and the surface conditions in both cases (the model experiments and this study) were similar, the samples used in the model experiments have a much larger overhang at the edges of the chip (the overhang is the distance from the periphery of the array to the edge of the package). If the area that showed weak adhesion (solder joint/flux area) was further away from the edge of the package, then the propensity for delamination seemed to decrease. In this case (the area of weak adhesion being away from the edge), the mechanical load due to the thermal stress is less, i.e. the mechanical load due to thermal stress goes down as the distance from the edge increases. This suggests that the reliability of the package can be enhanced by locating the I/Os away from the edge of the package. If the location of the I/Os is fixed, then the dimensions of the package can be increased to enhance the distance between the periphery of the array to the edge of the package. However, increasing the size of the package will increase its footprint on the assembly and the time needed for underfill. Besides, the samples used in the model experiments were over-cured. The longer curing time may be another reason for the reduced delamination.

The Delamination Interface

Typically, delamination occurred at the interface between the passivation layer and the underfill material. Delamination at this interface (passivation/encapsulant) is portrayed as a lighter region in the grey scale image generated by the SAM. This was confirmed by cross-sectioning several samples. However, the SAM images of the six samples that had a combination of SiO2 passivation, Flux I, and Encapsulant L (SIL) appear 뗒abnormal뛧 after 1000 cycles of thermal shock (Figure 5). An area that resembled a circle was observed at the center of the package. This area appears to be a dark region in the grey scale and seemed to have a tendency to increase during thermal cycling. This observation was different from the typical occurrence of delamination that was seen as a light region in a grey scale image. Through cross sectioning several samples, it was verified that the dark region in the grey scale image discussed above was indeed delamination at the interface between the silicon chip and the passivation layer.

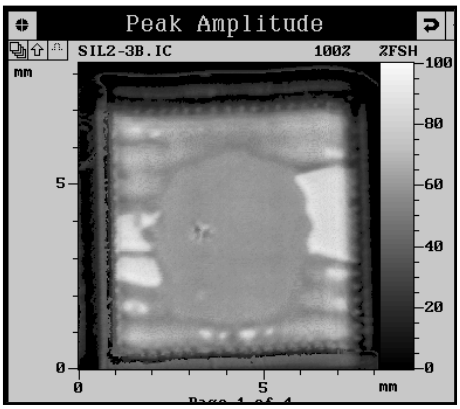

Figure 5. A SAM Image Which Appeared >Abnormal= after 1000 Cycles of Thermal Shock

The Floating of the Chip from the Underfill Material

For chips that have a polyimide passivation layer that were encapsulated using Encapsulant L, severe delamination occurred after 500 cycles and all the I/Os failed after 1000 cycles. For four out of six samples, the chip (with a polyimide passivation layer) fell off from the substrate during handling. The surface of the chip remained clean (no encapsulant residue). The underfill covered chip site on the substrate appeared shiny and no cracks were observed on the encapsulant. This indicated an absence of adhesion. A cross-section of one of these samples showed that the chip had lifted up for a distance of 7 mils (Figure 6). The chip's being lifted must have been caused by a force that is normal to the direction of the board. This (normal) force could be caused by the expansion of the moisture in the package (in either the board, solder mask, or passivation layer). A systematic study of the amount of moisture the packages have been exposed to is being conducted in a follow up experiment. While the edge of the chip was not passivated with polyimide, part of the encapsulant still adhered to the edge of the chip. Therefore, there were cracks in the encapsulant's fillet.

Besides, the cracks in the encapsulant were also observed at the corner of the chip (Figure 6).

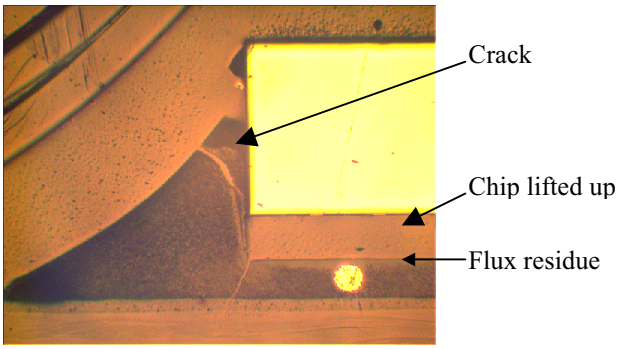

Figure 6. A Cross-Section Showing That a Chip Lifted up

COMPARISON BETWEEN THE MATERIALS USED

Passivation Layer Dependency

The degree of delamination was used as an indicator of package reliability. The delamination observed on the polyimide passivation surface was significantly more severe than the delamination observed on the SiO_2 passivation surface (Figures 7 and 8). This scenario was true for all three types of encapsulants that were studied. When Encapsulant L was used with a sample with a polyimide passivation, then 100% delamination was observed after 500 cycles. There was widespread electrical failure (69%) at this time. After 1000 cycles, all the interconnections failed. This indicated that after the underfill material did not provide adhesion, the solder joints were subject to thermal loads that eventually (a few hundred cycles later) resulted in cracks in the solder joints.

Underfill Material Dependency

Encapsulant L exhibited severe adhesion related problems especially when a polyimide passivation layer was used. These adhesion related problems resulted in delamination. Encapsulant E exhibited (relatively) better adhesion performance than Encapsulant J. The observed differences (delamination) between the three types of encapsulants was not significant after 500 cycles. However, after 1000 cycles, Encapsulant L again provided poorer results than the others with respect to delamination. While Encapsulants L and J exhibited similar performance after electrical testing, Encapsulant E appeared to be better.

Flux Dependency

While Flux H appears to provide relatively poorer results when compared with Flux K on a polyimide passivation surface, it (Flux H) appears to be slightly better than other fluxes on a SiO_2 passivation surface. As mentioned above, the failure mechanism (delamination) observed in this study was related to the presence of the flux residues. Flux K has a higher solids content (65%) and Flux I has a significantly lower solids content (5%). Both flux materials, however, exhibited similar performance with respect to the degree of delamination. These results indicate that the solids content of the flux (within the ranges tested) did not significantly impact the severity of the observed delamination.

The absence of flux dependency could be due to the scenario described below. The solids content may not be critical as long as the flux residue is spread onto the chip's surface. If the drum fluxer was used for fluxing prior to chip placement, it should be ensured that the active side of the chip remains uncontaminated. Flux tends to melt and soften at a higher temperature and should be able to wick up to the chip's surface. Flux residue was found to extend over a region about five mils around the solder joints (Figure 6). The flux could have climbed up to the chip surface during either substrate preheat (typically 75 °C) or encapsulant curing (around 150 °C). It was observed that the flux did not seem to climb up to the chip's surface at temperatures of either 70 °C or 90 °C. The flux must have climbed up to the chip's surface during encapsulant cure. The melting points of the various types of fluxes is usually around 80 °C. The slight difference in the melting points of the different fluxes was not expected to have an impact on the spread of the flux residue since all the melting points are much below the encapsulant curing temperature. Gelling the encapsulant material at a lower temperature (around 70 °C) before curing may prevent the flux residue from migrating.

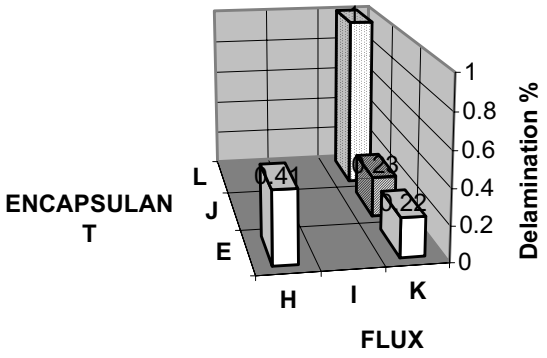

a. delamination After 500 Cycles of LLTS (polyimide passivation)

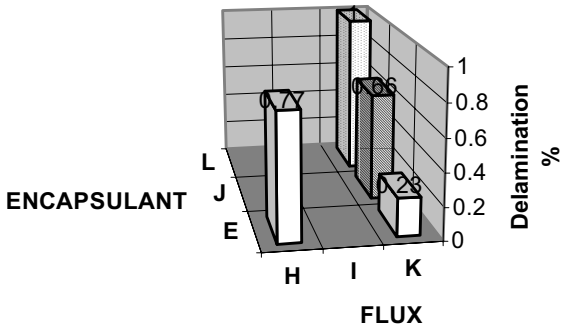

b. delamination After 1000 Cycles of LLTS (polyimide passivation)

Figure 7. The Precentages of Deliamination for Samples with a Polyimide Passivation Layor

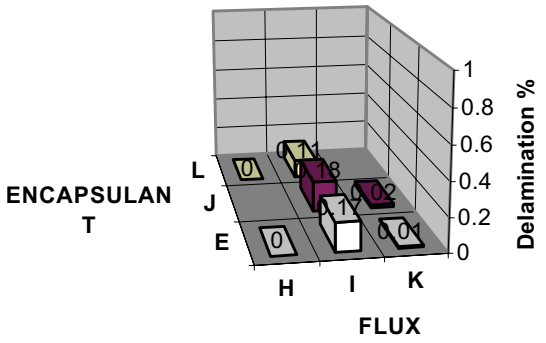

a. delamination After 500 Cycles of LLTS (SiO_2 passivation)

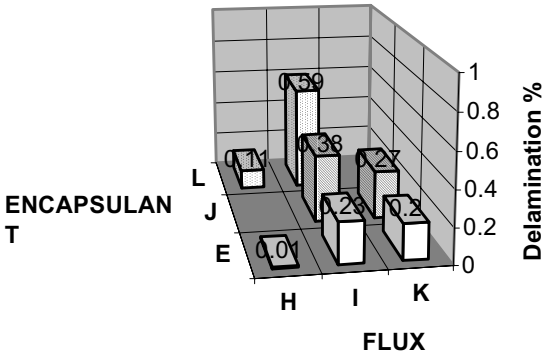

b. delamination After 1000 Cycles of LLTS (SiO_2 passivation)

Figure 8. The Precentages of Deliamination for Samples with a SiO_2 Passivation Layor

The Best Material Combination

The best combination of materials which resulted in the least amount of delamination and electrical failure seemed to be the chips with a SiO_2 passivation, fluxed by Flux H, and encapsulated using Encapsulant E. The results from electrical testing and the inspection for delamination support this inference on the best combination of materials. With this combination (chips with a SiO_2 passivation, fluxed by Flux H, and encapsulated using Encapsulant E), no delamination was observed after 500 cycles of thermal shock testing. The corresponding electrical failure rate was down to 0.7%. It needs to be kept in mind that actual electrical failures can be even lower if the metallurgy problems of the samples with a SiO_2 passivation are resolved. It is again emphasized here that the influence of the different types of flux used is not significant. With the same passivation (SiO_2) and underfill material (Encapsulant E), Flux K performs almost as good as Flux H. When Flux K was used, 1% delamination (on average) was seen in the samples after 500 cycles. The corresponding electrical failure rate was 5.1%.

CONCLUSION

The relative adhesion of three types of underfill materials on two types of passivation surfaces was evaluated. The majority of delamination began at the solder joint area due to the presence of flux residues. The delamination then extended inward towards the center of the chip.

All the three types of encapsulant materials exhibited better adhesion on the SiO_2 passivation surface than the polyimide passivation surface. The difference in the adhesion characteristics between the encapsulant materials was more significant when the surface was polyimide passivated. Encapsulant E exhibited superior adhesion performance while Encapsulant L exhibited severe adhesion problems especially on a polyimide passivation surface. Although the delamination mechanism was dominated by the presence of flux residues, the type of flux did not exhibit a significant influence on the degree of delamination.

The local warpage in the die area of the DCA package was discussed. This (the local warpage) was found to lead to the cracking of the silicon chip. Experiments were conducted to study the impact of pre-cure and annealing on the chip warpage. The reduction (in chip warpage) was not found to be significant. Data, however, suggested a systematic reduction of 10~15% by either pre-cure or annealing.

References

1. Jicun Lu, Jianhua Wu, Yih Pin Liew, Thiam Beng Lim, Xiangfu Zong, "The Impact of Underfill Properties on The Thermomechanical Reliability of FCOB Assembly," Soldering & Surface Mount Technilogy , (2000), pp.37-41.
2. Zhang Qun, Xie Xiaoming, Chen Liu , Wang Guozhong, Cheng Zhaonian, Wolfgang Kempe, "on the degradation of the solder joints of underfilled flip chip package : a caes study," Soldering & Surface Mount Technilogy , (2000), pp.24-28.
3. Jarmo Maattanen, Petteri Plam, Aulis Tuominen, Chen Liu, "Reliability of Flip Chip Component Soldered on FR5 Board ," Microelectronics International, (2000), pp.27-30.
4. F.P.McCluskey, L. Condra , T.Torri, J. Fink "Packaging Reliability for High Temperature Electronics : A Materials Focus," Microelectronics International, (1996), pp.23-26.
5. Gurumurthy,C.K, Warpage in the Area Array Microelectronic Devices, Master's Thesis, August 1996.

Singular Stress Analysis in a Viscoelastic Thin Layer Bonded to an Elastic Substrate Using Realistic Relaxation Function

Sang Soon Lee
Korea University of Technology and Education
School of Mechatronics Engineering
P.O.Box 55, Chonan, Chungnam, 330-600, South Korea
E-mail: sslee@kut.ac.kr

Abstract

This paper deals with the stress singularity induced at the interface corner between the perfectly bonded thin layer and elastic substrate subjected to a uniform temperature change and a shear loading using realistic relaxation function. The thin layer is assumed to be a linear viscoelastic material. The time-domain boundary element method is used to investigate the behavior of stresses for the whole interface. Within the context of a linear viscoelastic theory, a stress singularity exists at the point where the interface between one of the elastic substrate and the viscoelastic thin layer intersects the free surface.

1. Introduction

Polymeric materials such as polyimide or epoxy are extensively used in electronic industry as dielectric insulating layers and adhesive layers. Thin layers deposited on a substrate can be subjected to residual stresses due to difference in the thermal expansion coefficients. The mismatch in thermal properties between a thin layer and a substrate results in significant thermal stresses upon cool down from the cure temperature. It is well known that the interface of bonded quarter planes suffers from a stress system in the vicinity of the free surface under the external loading [1]. In such a region two interacting free surface effects occur, and singular interface stresses can be produced.

The viscoelastic interface problems have been studied by several investigators. Weitsman[2] analyzed the mechanical behavior of an epoxy adhesive layer as the adhesive absorbs moisture from the ambient environment. Delale and Erdogan[3] presented the viscoelastic behavior of an adhesively bonded lap joint. Lee[4,5] performed the boundary element analysis of the stress singularity for the viscoelastic adhesive layer. Because the order of the singularity is material-dependent, it tends to change with time in viscoelastic materials.

In this study, the stress singularity at the interface corner between a substrate and a viscoelastic layer subjected to the uniform temperature change is investigated. The substrate is considered as rigid since it is much stiffer than the viscoelastic layer. The boundary element method(BEM) is employed to investigate the interface stresses in the viscoelastic thin layer.

2 . The Stress Singularity

The order of the stress singularity at the interface corner between the substrate and the viscoelastic layer can be determined using a method similar to that described by Lee[4,5] and Williams[6]. The substrate is assumed to be rigid. Fig.1 shows the region near the interface corner between perfectly bonded viscoelastic and rigid quarter planes. The free surfaces are assumed to be traction free.

Polymeric layers used in electronic packages are extremely thin, with the thickness rarely exceeding $50\mu m$. For sufficiently thin layer it is possible to neglect the temperature gradient through the thickness and consider the transient case of uniform temperature $T(\mathbf{x},t)=T(t)$.

In the following, a condition of plane strain is considered. A solution of

$$\nabla^4\phi(r,\theta;\xi)=0 \tag{1}$$

is to be found such that the normal stress, $\sigma_{\theta\theta}$, and shear stress, $\tau_{r\theta}$,vanish along $\theta=\pi/2$, further that the displacements are zero across the common interface line $\theta=0$. In eqn (1) , ξ is the *reduced time* defined as follows:

$$\xi=\xi(t)=\int_0^t A_T(T(\rho))d\rho \tag{2}$$

where A_T is the shift function, a function of temperature history.

In the present study, a constant temperature change $\Delta TH(t)$ is considered. Here $H(t)$ represents Heaviside unit step function. This simple field is considered in order to allow the study to focus on the effects of viscoelastic behavior on the singular stress field. Under the constant temperature change $\Delta TH(t)$, the reduced time ξ of eqn (2) becomes

$$\xi=A_T t \tag{3}$$

The solution of this problem can be facilitated by the Laplace transform. With temperature change $\Delta TH(t)$ in the viscoelastic layer, it is convenient to use the Laplace transform with respect to reduced time ξ , instead of *real time* t . Then, eqn (1) can be rewritten as follows:

$$\nabla^4\phi^*(r,\theta;s)=0 \tag{4}$$

where ϕ^* denotes the Laplace transform of ϕ with respect to ξ and s is the transform parameter.

Using a method similar to that described by Lee[4,5], the

transformed characteristic equation is obtained as follows:

$$\frac{2\lambda^2}{s} - 8s\left[\nu^*(s)\right]^2 + 12\nu^*(s) - \frac{5}{s} - \left[\frac{3}{s} - 4\nu^*(s)\right]\cos(\lambda\pi) = 0 \tag{5}$$

where λ is the stress singularity parameter and s is the transform parameter. $\nu^*(s)$ is Laplace transform of the viscoelastic Poisson's ratio $\nu(\xi)$. The time dependent behavior of the problem is recovered by inverting eqn (5) into the time space.

The singularity at the interface corner has a form of $r^{1-\lambda}$. Roots of eqn (5) with $0 < \mathrm{Re}(\lambda) < 1$ are of main interest. The calculation of the zeros of eqn (5) can be carried out numerically for given values of material properties. For $0 < \nu(\xi) < 0.5$, there is at most one root λ with $0 < \mathrm{Re}(\lambda) < 1$, and that root is real[1].

3. Boundary Element Analysis of the Interface Stresses

A viscoelastic thin layer bonded to a rigid substrate is shown in Fig.2(a). The free surfaces of Fig.2(a) are traction-free and the uniform temperature change provides the only loading. The thin layer has thickness h and length $2L$. Due to symmetry, only one half of the layer needs to be modeled. Fig. 2(b) represents the two-dimensional plane strain model for analysis of the interface stresses between the viscoelastic layer and the substrate. Calculations are performed for $L/h = 25$

A uniform temperature change $\Delta TH(t)$ in the viscoelastic layer is equivalent to increasing the tractions by $\gamma(t)n_j$ [7]where

$$\gamma(t) = 3K\alpha\Delta TH(t) \tag{6}$$

Here, K is the bulk modulus; n_j are the components of the unit outward normal to the boundary surface; and α is the coefficient of thermal expansion of the viscoelastic layer.

With a uniform temperature change in the layer, it is convenient to write the boundary integral equations with respect to *reduced time* ξ , instead of *real time* t . Then, the boundary integral equations without any other body forces are written as follows:

$$\begin{aligned}
&c_{ij}(\mathbf{y})u_j(\mathbf{y},\xi) \\
&+ \int_S \left[u_j(\mathbf{y}',\xi)T_{ij}(\mathbf{y},\mathbf{y}';0+) + \int_{0+}^{\xi} u_j(\mathbf{y}',\xi-\xi')\frac{\partial T_{ij}(\mathbf{y},\mathbf{y}';\xi')}{\partial\xi'}d\xi' \right] dS\ (\mathbf{y}') \\
&= \int_S \left[t_j(\mathbf{y}',\xi)U_{ij}(\mathbf{y},\mathbf{y}';0+) + \int_{0+}^{\xi} t_j(\mathbf{y}',\xi-\xi')\frac{\partial U_{ij}(\mathbf{y},\mathbf{y}';\xi')}{\partial\xi'}d\xi' \right] dS\ (\mathbf{y}') \\
&+ \int_S \left[\gamma\ (\xi)n_j U_{ij}(\mathbf{y},\mathbf{y}';0+) + \int_{0+}^{\xi} \gamma\ (\xi-\xi')n_j\frac{\partial U_{ij}(\mathbf{y},\mathbf{y}';\xi')}{\partial\xi'}d\xi' \right] dS\ (\mathbf{y}')
\end{aligned} \tag{7}$$

where u_j and t_j represent displacement and traction, and S is the boundary of the given domain. $c_{ij}(\mathbf{y})$ is dependent only upon the local geometry of the boundary. For $\mathbf{y}$ on a smooth surface, the free term $c_{ij}(\mathbf{y})$ is simply a diagonal matrix $0.5\delta_{ij}$. The viscoelastic fundamental solutions, $U_{ij}(\mathbf{y},\mathbf{y}';\xi)$ and $T_{ij}(\mathbf{y},\mathbf{y}';\xi)$, can be obtained by applying the elastic-viscoelastic correspondence principle to Kelvin's fundamental solutions of linear elasticity.

A closed form integration of eqn (7) is not possible and therefore numerical quadrature must be used. Eqn (7) can solved in a step by step fashion in time by using the modified Simpson's rule for the time integrals and employing the standard BEM for the surface integrals. Eqn (7) can be rewritten in matrix form to give the global system of equations:

$$[\mathbf{H}]\{\mathbf{u}\} = [\mathbf{G}]\{\mathbf{t}\} + \{\mathbf{B}_T + \mathbf{R}\} \tag{8}$$

where $\mathbf{H}$ and $\mathbf{G}$ are the influence matrices; $\mathbf{B}_T$ is the known input due to temperature change; $\mathbf{R}$ is the hereditary effect due to the viscoelastic history. Solving eqn (8) under boundary conditions leads to determination of all boundary displacements and tractions. The solutions are obtained in terms of reduced time ξ . The final solutions are then obtained by converting to real time t .

4. Numerical Results

An epoxy material has been selected as being a viscoelastic layer of significant current technical interest. The numerical calculations are based on the experimental data for epoxy[8]

$$\begin{aligned}
E(t) &= \frac{3.2\times10^3}{1+0.0336\,t^{0.19}} \quad MPa \qquad (t;\ \mathrm{min}) \\
K(t) &= K_0 = 3.556\times10^3 \quad MPa
\end{aligned} \tag{9}$$

where K is the bulk modulus and E is the tensile relaxation modulus.

In order to solve the boundary element equation (8), the viscoelastic fundamental solutions, U_{ij} and T_{ij} should be known. Such viscoelastic fundamental solutions can be obtained by applying the correspondence principle to the elastic fundamental solutions. The relaxation function $E(t)$, as given in eqn (9), is complex that the Laplace transform of tensile relaxation function cannot be determined precisely. To reduce the computational effort significantly, the method of collocation is employed and the relaxation function $E(t)$ is expanded as

$$E(t) = E_0 + \sum_{n=1}^{14} \exp\left[-\frac{t}{\beta_i}\right] \tag{10}$$

The values of E_i and β_i are listed in Table 1. The viscoelastic fundamental solutions U_{ij} and T_{ij} for the relaxation function given by eqn (10) are obtained numerically by using elastic-viscoelastic correspondence principle. The detailed calculation procedure is provided in ref.[9].

Table 1. The constants of eqn (10)

β_i (min)	E_i (MPa)
0.5 x 10^{14}	0.10817 E+03
0.5 x 10^{13}	0.12935 E+03
0.5 x 10^{12}	0.18168 E+03
0.5 x 10^{11}	0.23739 E+03
0.5 x 10^{10}	0.28994 E+03
0.5 x 10^{9}	0.32514 E+03
0.5 x 10^{8}	0.33116E+03
0.5 x 10^{7}	0.30568 E+03
0.5 x 10^{6}	0.25760 E+03
0.5 x 10^{5}	0.20145 E+03
0.5 x 10^{4}	0.14720 E+03
0.5 x 10^{3}	0.10934 E+03
0.5 x 10^{2}	0.48615 E+02
0.5 x 10	0.15854 E+03
———	E_o= 0.16876 E+03

The viscoelastic layer $\left(\alpha = 4.3\times10^{-5}/^{o}C\right)$ is assumed to be stress-free at a temperature of $150^{o}C$ and is cooled suddenly from a cure temperature down to room temperature $\left(23^{o}C\right)$. The boundary element discretization consisting of 23 line elements was employed. The refined mesh was used near the interface corner. Quadratic shape functions were used to describe both the geometry and functional variations. Viscoelastic stress profiles were plotted along interface to investigate the nature of stresses. Fig. 3 and Fig.4 show the distribution of normal stress σ_{yy} and shear stress τ_{xy} on the interface at $t = 0$ and 8 hr. The numerical results exhibit the relaxation of interface stresses and large gradients are observed in the vicinity of the free surface. Such residual thermal stress may cause interface delamination in the absence of applied external loads.

5. Conclusions

The stress singularity induced at the interface corner between the viscoelastic layer and the rigid substrate due to temperature change has been investigated. The interface stresses have been calculated using BEM. An epoxy material has been selected as being a viscoelastic layer of significant current technical interest. The numerical calculations are based on the experimental data for epoxy. Since it is highly inconvenient to obtain the Laplace transform of the relaxation function of realistic viscoelastic materials, the method of collocation has been employed and the relaxation function has been expanded in a sum of exponentials. The transformed viscoelastic fundamental solutions have been obtained using the correspondence principle and the inversion of transformed functions has been performed numerically. Thermal residual stresses developed during cooling from an elevated cure temperature down to room temperature are large enough to initiate interface delamination to relieve the residual stresses. All results reported here are for $L/h = 25$, and are applicable to layers that behave as if they are semi-infinite.

References

1. Bogy, D.B., "Edge-bonded dissimilar orthogonal elastic wedges under normal and shear loading", *ASME Journal of Applied Mechanics*, 35 (1968), pp. 460-466 .
2. Weitsman, Y., " Interfacial stresses in viscoelastic adhesive layers due to moisture sorption," *International Journal of Solids and Structures*, 15(1979), pp. 701-713 .
3. Delale, F. and Erdogan F. , 1981, "Viscoelastic analysis of adhesively bonded joints", *ASME Journal of Applied Mechanics*, 48 (1981) pp.331-338 .
4. Lee, S.S., " Boundary element analysis of the stress singularity at the interfacecorner of viscoelastic adhesive layers, *International Journal of Solids and Structures*," 35 (1998), pp.1385-1394 .
5. Lee, S.S., " Boundary element analysis of the singular hygrothermal stresses in a bonded viscoelastic thin film ", *International Journal of Solids and Structures*," 38 (2001), pp.401-412 .
6. Williams, M.L., 1952, " Stress singularity resulting from various boundary conditions in angular corners of plates in extension," *ASME Journal of Applied Mechanics*, 74 (1952), pp.526-528.
7. Lee, S.S. and Westmann, R.A., "Application of high-order quadrature rules to time domain boundary element analysis of viscoelasticity," *International Journal for Numerical Methods in Engineering*, 38 (1995), pp. 607-629 .
8. Weitsman, Y. "Residual thermal stresses due to cool-down of epoxy-resin composite" *ASME Journal of Applied Mechanics*, 46 (1979), pp. 563-567.
9. Lee, S.S. "Boundary element analysis of linear viscoelastic problems using realistic relaxation functions" *Computers and Structures*, 55 (1995), pp. 1027-1036.

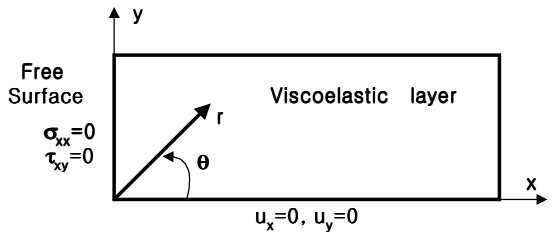

Fig. 1 Interface corner of thin layer

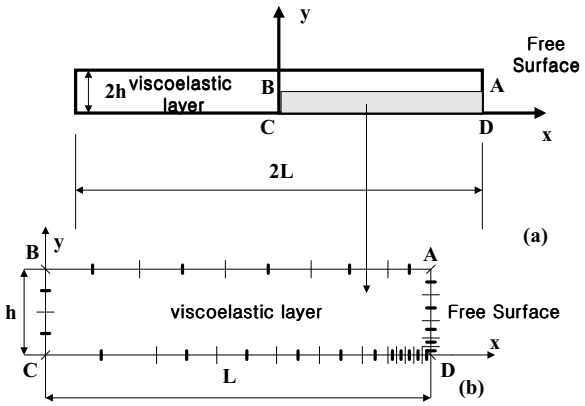

Fig. 2 Boundary element modelling

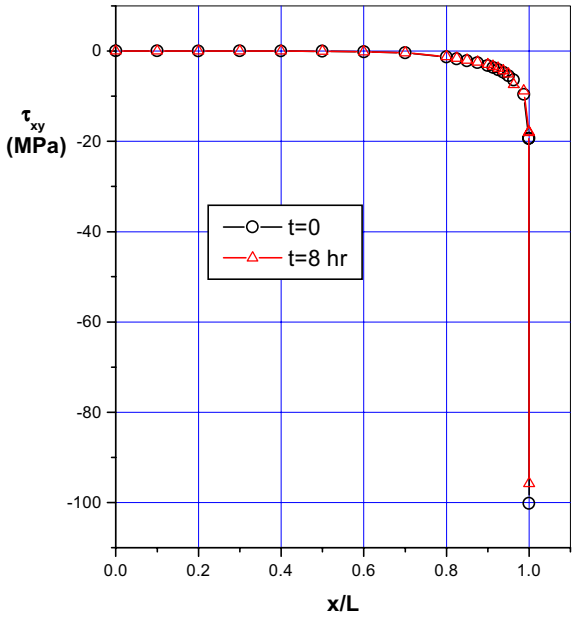

Fig. 4 Interface shear stresses τ_{xy}

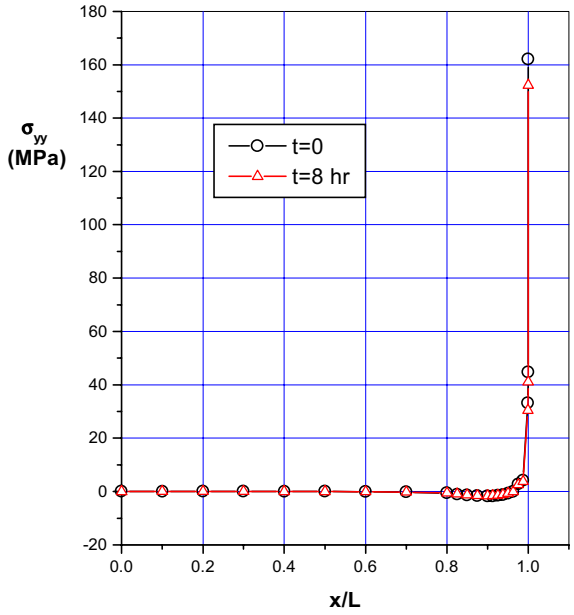

Fig. 3 Interface normal stresses σ_{yy}

Analysis of Three Dimensional Crack Corners via Conservation Integral

Yongwoo Lee*, Dong-Won Jung** and Seyoung Im*
*Mechanical Engineering, Korea Advanced Institute of Science and Technology,
Science Town, Taejeon, S. Korea, lyw@imhp.kaist.ac.kr, sim@kaist.ac.kr
**Mechanical Engineering, Cheju National University, Cheju, S. Korea, jdwcheju@cheju.cheju.ac.kr

Abstract

With the aid of the two-state M-integral and finite element analysis, the asymptotic solution in terms of the complete eigenfunction expansion is obtained for three dimensional crack corner problems. The proposed scheme enables us to extract the intensity of the eigenfunction term from the far field data without resort to special singular elements at the vertex.

Introduction

Since a general numerical procedure to determine three dimensional stress ginguarities was first developed by Bazant and Estenssoro[1] for isotropic elastic material, many studies[2-12] have been directed to compute the order of the stress singularities at various three dimensional corner geometries in bimaterial materials as well as homogeneous materials. Some researchers developed new numerical procedures to compute the stress singularities, for example, BEM[9], boundary integral equation method[10]]. However, these earlier works have concentrate on the stress singularities at the intersecton of a crack with a free surface which are different that the classical $r^{-1/2}$ singularity while only a few studies had tried to compute the stress intensities as well as the stress singularities of the given problem. Nakamura and Parks[13] introduced the corner stress intensity factor and related the corner stress itensity factor with the stress intensity factors in a thin elastic plate. Recently, Labossiere and Dunn[12] proposed an approach to compute the stress intensities and to correlate fracture initiation at three dimensional bimaterial interface corners.

In this work, we are conerned with applications of a conservation law for computing the stress intensity for three dimensional crack corners. The conservation law was derived from the M-integral by chen and Shield[14]. It is the interaction of M-integral between two equillibrium elastic states and so may be termed 'two-state Mintegral'. Im and Kim[15] showed that the two-state M-integral is applicable for computing the intensity of singlar near-tip stress for a two dimensional generic wedge. They proved the existence of the so-called complementary eigenfunction in the M-integral sense for every eigenfunction in the eigenfunction solution for two dimensional generic wedge problems. Utilizing the two-state M-itnegral and the complementarity of the eigenvalues Lee et al.[16] computed the stress intensity for a adhesive lap joint. In addition, The existence of the complementary eigenvalues in the M-integral sense for three dimensional generic wedge problems was verified numerically by Im and Lee[17].

3-D stress singularity

For the purpose of an asymptotic analysis for possible stress singularities at the vertex of generic wedges we introduce separable displacement solutions of the form

$$\begin{aligned} u &= \beta_s r^{\lambda}\tilde{u}(\theta,\phi;\lambda) \\ v &= \beta_s r^{\lambda}\tilde{v}(\theta,\phi;\lambda) \\ w &= \beta_s r^{\lambda}\tilde{w}(\theta,\phi;\lambda) \end{aligned} \qquad (1)$$

where r, θ and ϕ are the spherical coordinates, (u, v, w) are the components of displacement in (r, θ, ϕ) directions, respectively. Values of λ are called eigenvalues and its corresponding functions $\tilde{u}(\theta,\phi;\lambda)$, $\tilde{v}(\theta,\phi;\lambda)$ and $\tilde{w}(\theta,\phi;\lambda)$ are called eigenfunctions. This displacement field is required to satisfy equations of equilibrium within the conical region and the proper homogeneous boundary conditions on the lateral surface as shown Fig. 1. When displacements are of the form given by Eq. (1) the stresses are proportional to $r^{\lambda-1}$. Hence a stress singularity occurs at the origin when $\mathrm{Re}(\lambda) < 1$. On the other hand, the boundedness of the strain energy at the origin requires $\mathrm{Re}(\lambda) > -1/2$. However, $\mathrm{Re}(\lambda) < 0$ implies that the displacements are unbounded at r=0, which is physically unrealistic except for applying a concentrated load at the vertex. Therefore we are primarily interested in eigenvalues λ in the range $0 < \mathrm{Re}(\lambda) < 1$.

In order to evaluate the stress singularity λ, Bazant and Estenssoro[1] developed a finite element scheme based upon a variational principle. The problem of calculating the stress singularity is reduced to an eigenvalue problem for λ with the eigenfucntion represented by displacements or stresses on the unit sphere surrounding the vertex.

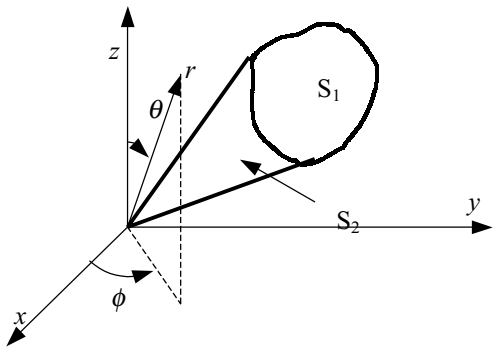

Fig. 1. Three dimensional conical notch and the associated spherical coordindate system.

For the conical solid shown in Fig. 1 the two boundaries are $r=r_0$ and $\psi(\theta,\phi)=0$ and are denoted by S_1 and S_2, respectively. We can write the principle of minimum potential energy as(for detail see Ref. 5)

$$\delta U - \int_{S_1} (t_r \delta u + t_\theta \delta v + t_\phi \delta w) r^2 \sin\theta d\theta d\phi = 0 \qquad (2)$$

where

$$U = \int_V \Phi dr d\theta d\phi$$

is the total strain energy in the volume V of the cone a y nd

$$\Phi = E r^2 \sin\theta$$

where E is the strain energy density. E is a function of the strain and they in turn are functions of the displacements and their first derivatives. Therefore we get

$$\begin{aligned}\delta U = \int_V (&\Phi_{,u}\delta u + \Phi_{,u_r}\delta u_r + \Phi_{,u_\theta}\delta u_\theta + \Phi_{,u_\phi}\delta u_\phi \\ &+\Phi_{,v}\delta v + \Phi_{,v_r}\delta v_r + \Phi_{,v_\theta}\delta v_\theta + \Phi_{,v_\phi}\delta v_\phi \\ &+\Phi_{,w}\delta w + \Phi_{,w_r}\delta w_r + \Phi_{,w_\theta}\delta w_\theta + \Phi_{,w_\phi}\delta w_\phi) dr d\theta d\phi \end{aligned} \qquad (3)$$

where the subscripts r, θ and ϕ denote partial differentiation and comma also the partial differentiation. The eigenfunction need not satisfy the far field boundary conditions on S_1. Therefore we will modify Eq. (2) into a form that would allow far-field boundary conditions to be separated out from the others. Substituting Eq. (3) into Eq. (2) and integrating the terms containing δu_r, δv_r and δw_r by parts in the r-direction, Eq. (2) can be rewritten as:

$$\begin{aligned}\delta\overline{U} + \int_{S_1} (&\Phi_{,u_r}\delta u + \Phi_{,v_r}\delta v + \Phi_{,w_r}\delta w) d\theta d\phi \\ &- \int_{S_1} (t_r \delta u + t_\theta \delta v + t_\phi \delta w) r^2 \sin\theta d\theta d\phi = 0 \end{aligned} \qquad (4)$$

where

$$\begin{aligned}\delta\overline{U} = \int_V [&\{\Phi_{,u} - \frac{\partial}{\partial r}(\Phi_{,u_r})\}\delta u + \Phi_{,u_\theta}\delta u_\theta + \Phi_{,u_\phi}\delta u_\phi \\ &\{\Phi_{,v} - \frac{\partial}{\partial r}(\Phi_{,v_r})\}\delta w + \Phi_{,v_\theta}\delta w_\theta + \Phi_{,v_\phi}\delta v_\phi \\ &\{\Phi_{,w} - \frac{\partial}{\partial r}(\Phi_{,w_r})\}\delta w + \Phi_{,w_\theta}\delta w_\theta + \Phi_{,w_\phi}\delta w_\phi] dr d\theta d\phi \end{aligned}$$

The terms concerned with the boundary S_2 vanish due to traction free condition or rigid constraint.

Thus, Eq. (2) can be expressed as:

$$\begin{aligned}\delta\overline{U} + \int [&(\sigma_{rr} - t_r)\delta u + (\sigma_{r\theta} - t_\theta)\delta v \\ &+ (\sigma_{r\phi} - t_\phi)\delta w] r^2 \sin\theta d\theta d\phi = 0 \end{aligned}$$

which implies

$$\begin{aligned}&\delta\overline{U} = 0, \\ &\sigma_{rr} = t_r,\ \sigma_{r\theta} = t_\theta,\ \sigma_{r\phi} = t_\phi \qquad \text{on } S_1. \end{aligned} \qquad (5)$$

Since we assume that the traction on S_1 is denoted by (t_r, t_θ, t_ϕ), we come to the conclusion that Eq. (5) is a variational statement that would ensure the satisfaction of the equations of equilibrium in V and the boundary conditions on S_2 only.

Let the stresses and the strains be represented by 1-D arrays as follows:

$$(\sigma_1,\sigma_2,\sigma_3,\sigma_4,\sigma_5,\sigma_6) = (\sigma_{rr},\sigma_{\theta\theta},\sigma_{\phi\phi},\sigma_{\theta\phi},\sigma_{r\phi},\sigma_{r\theta})$$

$$(\varepsilon_1,\varepsilon_2,\varepsilon_3,\varepsilon_4,\varepsilon_5,\varepsilon_6) = (\varepsilon_{rr},\varepsilon_{\theta\theta},\varepsilon_{\phi\phi},2\varepsilon_{\theta\phi},2\varepsilon_{r\phi},2\varepsilon_{r\theta})$$

Material constitutive relation is

$$\sigma_i = C_{ij}\varepsilon_j \qquad (6)$$

where i, j =1~6 and C_{ij} is the material stiffness which satisfies $C_{ij}=C_{ji}$.

To derive the expressions for a finite element formulation, let the area containing material boundary by the curve $\psi(\theta, \phi)=0$ on (θ, ϕ) plane be denoted by A, and let it be subdivided into an n number of finite elements. Using the isoparametric concept, we have

$$\theta=N_i\theta_i, \quad \phi=N_i\phi_i \qquad (i=1\sim6)$$

where θ_i and ϕ_i are the nodal values of these variables. Let $\mathbf{x}$ be the vector of nodal degree of freedom associated with a typical element and define interpolation function $\mathbf{U}(\theta, \phi)$, $\mathbf{V}(\theta, \phi)$ and $\mathbf{W}(\theta, \phi)$ by

$$\begin{aligned}&\tilde{u}(\theta,\phi) = U^i(\theta,\phi)x_i \\ &\tilde{v}(\theta,\phi) = V^i(\theta,\phi)x_i \\ &\tilde{w}(\theta,\phi) = W^i(\theta,\phi)x_i \end{aligned} \qquad (7)$$

where i=1~27, $\mathbf{U}$=(N_1, 0, 0, N_2, …), $\mathbf{V}$=(0, N_1, 0, …), $\mathbf{W}$=(0, 0, N_1, …) and $\mathbf{x}$=(u_1, v_1, w_1, u_2, ….).

Applying Eq. (7) and (6) into Eq. (5), the first term in Eq. (5) is reduced to the eigenvalue problem(for detail see Ref. 5-8). The eigenvalue problem for λ is quadratic, i.e., of the form $(\mathbf{K} + \lambda\mathbf{D} + \lambda^2\mathbf{M})\mathbf{x} = \mathbf{0}$. To calculate λ by the Muller method,

it is necessary to repeatedly compute $\left\|\mathbf{K}+\lambda\mathbf{D}+\lambda^2\mathbf{M}\right\|$ for various λ values.

Finite element mesh consists of 2-D 8-node isoparametric quadrilateral elements. Numerical integration is performed using Gauss quadrature rule on a grid of $n_G \times n_G$ integration points. In a general anisotropic material the material stiffness matrix C_{ij} are functions of θ and ϕ and at every integration point they have to be evaluated. The transformation is that corresponding to a fourth order tensor and the transformation matrix contains terms like $\cos\theta$, $\cos\phi$, $\sin\theta$ and $\sin\phi$. Therefore C_{ij} will display a strong dependence on these terms and their higher powers. The strains also contain these trigonometric functions. Examination of the expressions involved shows that terms like $1/\sin\theta$ are present. This leads to some difficulties numerically in evaluating the integral accurately, especially in the region near the pole of the coordinate system where $\theta \cong 0$. Since a prior estimate of the number of integration points is not possible, the choice of integration points has to be based on numerical testing.

Application of the two-state M-integral

M-integral can be generally written as[18]:

$$M=\int_S\{Wx_in_i-t_iu_{i,k}x_k+\frac{m-n}{m}t_iu_i\}dS \tag{8}$$

where W and t_i indicate the strain energy density and the traction component, given as $W=\frac{1}{2}C_{ijkl}\varepsilon_{ij}\varepsilon_{kl}$ and $t_i=\sigma_{ij}n_j$, and u_j is the displacement component. m is the degree of homogeneity of the strain energy density that is 2 for the linear elastic problem when the strain energy density can be given as $W=\frac{1}{2}C_{ijkl}\varepsilon_{ij}\varepsilon_{kl}$ and n is the degree of freedom of the spatial dimension, e.g., n is equal to 2 for two-dimensional problems or 3 for three-dimensional problems. Thus M-integral for three dimensional problems can be rewritten as:

$$M=\int_S\{Wx_in_i-t_iu_{i,j}x_j-\frac{1}{2}t_iu_i\}dS \quad (i,j=1,2,3)$$

Suppose two independent elastic states, "A" and "B". We consider another elastic state "C" obtained by superposing the two equilibrium states A and B. Then the above M-integral is written as

$$M^C=M^A+M^B+M^{(A,B)} \tag{9}$$

where the superscripts A, B and C indicate the aforementioned elastic states, and $M^{(A,B)}$ is the two-state M-integral, given as :

$$M^{(A,B)}=\int_S[C_{ijkl}\varepsilon_{ij}^A\varepsilon_{kl}^Bn_px_p-(t_i^Au_{i,p}^B+t_i^Bu_{i,p}^A)x_p$$
$$+\frac{m-n}{m}(t_i^Au_i^B+t_i^Bu_i^A)]dS \tag{10}$$

The integral $M^{(A,B)}$, associated with the M-integral, results from the mutual interaction between the two elastic states A and B. This integral is referred to as the two-state M-integral in this context. The two-state M-integral for three dimensional problems can be rewritten as:

$$M^{(A,B)}=\int_S[C_{ijkl}\varepsilon_{ij}^A\varepsilon_{kl}^Bn_px_p-(t_i^Au_{i,p}^B+t_i^Bu_{i,p}^A)x_p$$
$$-\frac{1}{2}(t_i^Au_i^B+t_i^Bu_i^A)]dS$$

Moreover, $M^{(A,B)}$ is the conservation integral for two equilibrium states since these contour integrals identically vanish for the domains with no singularities.

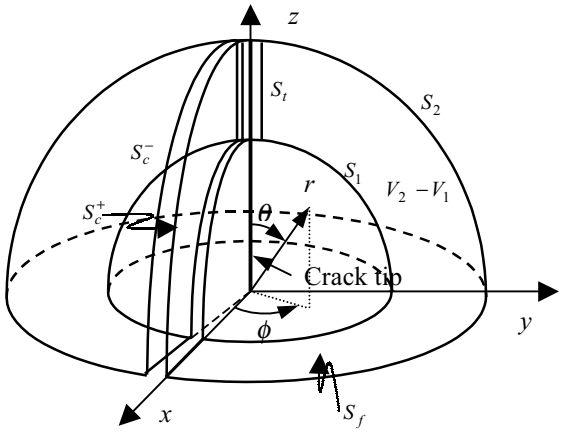

Fig. 3 Closed contour to derive the path-independence of the M-integral

Recalling that the M-integral is dependent on the origin of the Cartesian coordinate system, we take its origin at the crack corner at which the crack tip meets the free surface as shown in Fig. 3. Consider two surface contours in Fig. 3. Noting that the value of M-integral for elastic fields free from singlarities is equal to zero, we see that the path-independence of the M-integral derived from the vanishing of M-integral for the closed contour $S_2-S_t+S_c^+ +S_c^- -S_1+S_f$:

$$M(S_1)=M(S_2)-M(S_t)$$

where $M(S_c^+)=M(S_c^-)=M(S_f)=0$ and $M(S_1)=-M(-S_1)$ have been used. The second term $M(S_t)$ is the effect of the crack tip singularity and calculated on the surface S_t along the crack tip line. However, though the another stress singularity $1/\sqrt{x^2+y^2}$ which corresponds to the stress singularity of the plane crack problems exists along the crack

tip line, we can prove that $M(S_t)$ is identically equal to zero. Moreover, the path-independence of the two-state M-integral $M^{(A,B)}$ is apparent from the above and Eq. (9) and can be written as :

$$M^{(A,B)}(S_1) = M^{(A,B)}(S_2) - M^{(A,B)}(S_t) \tag{11}$$

where the second term $M^{(A,B)}(S_t)$ can be written as :

$$M^{(A,B)}(S_t) = \lim_{\rho \to 0} \int_{S_t} \{ W^{(A,B)} x_i n_i - t_i^{(A)} \frac{\partial u_i^{(B)}}{\partial x_j} x_j - t_i^{(B)} \frac{\partial u_i^{(A)}}{\partial x_j} x_j - \frac{1}{2} t_i^{(A)} u_i^{(B)} - \frac{1}{2} t_i^{(B)} u_i^{(A)} \} r \sin\theta dr d\phi \tag{12}$$

where $\rho = \sqrt{x^2 + y^2}$ is distance from the crack tip line. If ρ decreases into zero, the asymptotic solutions reveal the the plane crack field solutions and then we can also prove that $M^{(A,B)}(S_t)$ is identically equal to zero. Thus the path-independence of the two-state M-integral for three dimensional crack corner problems can be obtained by computing only the two terms in Eq. (11).

The accurate computation of the two-state M-integaral $M^{(A,B)}$ on the far field is possible just via a regular displcement based FEM in connection with the domain integral representation. Now untilizing the domain integral representation and going through some manipulation, we can reach the following expression :

$$M^{(A,B)} = \int_{V_2 - V_1} [C_{ijkm} \varepsilon_{ij}^A \varepsilon_{km}^B x_l - (\sigma_{li}^A u_{i,p}^B + \sigma_{li}^B u_{i,p}^A) x_p - \frac{1}{2} (\sigma_{li}^A u_i^B + \sigma_{li}^B u_i^A)] q_{,l} dS \tag{13}$$

whre V_1 and V_2 represent the domain inside the surface S_1 and S_2 , respectively and $V_2 - V_1$ indaicates the region surrounded by S_1 and S_2 as shown in Fig. 3; the function $q(x_1, x_2, x_3)$ is a weight function that is defined to be 1 on S_2 and to be 0 on S_1 with smooth variation between S_1 and S_2. Then Eq. (13) is also conserved for an arbitary banded volume $V_2 - V_1$.

For an arbitrary eigenvalue λ in Eq. (1), we first define its complementary eigenvalue λ^c for three dimensional problems in the M-integral sense such that

$$\lambda + \lambda^c = -1$$

where λ^c constitutes another eigenvalue as long as λ belongs to the eigenvalues for a given problem[4]. The existence of the complementary relation of eigenvalues for two dimensional problems was verified by Leguillon and Sanchez-Palencia[19], and recently by Im and Kim[15] with the aid of energetics argument associated with the M-integral. The existence of the complementary eigenvalue for three dimensional problems is verified numerically in next section. The elastic state for the complementary eigenvalue λ^c , with its intensity β_l^c , may be written as :

$$\begin{aligned} u &= \beta_s^c r^{\lambda} \tilde{u}(\theta, \phi; \lambda^c) \\ v &= \beta_s^c r^{\lambda} \tilde{v}(\theta, \phi; \lambda^c) \\ w &= \beta_s^c r^{\lambda} \tilde{w}(\theta, \phi; \lambda^c) \end{aligned} \tag{14}$$

We now consider the superposition of the above complementary elastic state on the given elastic state for three dimensional crack corner under consideration. To calculate $M^{(A,B)}$ near the crack corner we substitute the elastic field (1) for the elastic state (A), and the complementary field (14) for the elastic state (B). the the following expression can be obtained for the two-state M-integral $M^{(A,B)}$

$$\begin{aligned} M_{\Gamma}^{(A,B)} &= \int_S \beta_s \beta_s^c r^{\lambda + \lambda^c - 1} \cdot F(\theta, \phi; \lambda, \lambda^c) \cdot r^2 \sin\theta d\theta d\phi \\ &= \int_S \beta_s \beta_s^c r^{\lambda + \lambda^c + 1} \cdot F(\theta, \phi; \lambda, \lambda^c) \sin\theta \cdot d\theta d\phi \end{aligned} \tag{15}$$

where $F(\theta, \phi; \lambda, \lambda^c)$ is computed by some tedius manipulation and expressed as a very complex form. Thus the detail form of $F(\theta, \phi; \lambda, \lambda^c)$ is omitted in this paper.

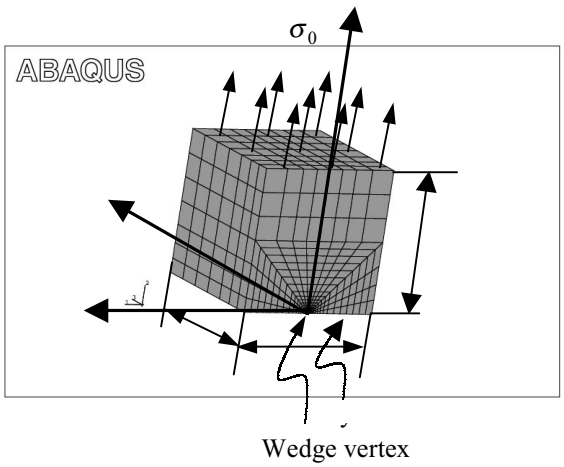

Fig. 4. Finite element mesh of the half model and boundary conditions

Numerical example

We consider the crack corner region of a thick plate remotely subjected to symmetric loading conditions as shown in Fig. 4. Now since we consider only the symmetric loading, we take the half model and its finite element mesh is shown in

Fig. 4. The length in x-axis, y-axis and z-axis, respectively is L and the crack length is L/2. We take the origin into the corner where the crack tip line intersects with the free surface. The crack surface is $x > 0$ and $z \geq 0$ in the x-z plane and symmetric boundary conditions are applied to the ligament plane, $x \leq 0$ and $z \geq 0$ in the x-z plane. Finite element analysis has been carried out using the package code ABAQUS. The finite element mesh consists of 20-node isoparametric brick elements. The mesh near the crack corner is refined due to the presence of the singularity.

At a point sufficiently close to the three dimensional crack corner the asymptotic deformation field should be characterized by the stress singularity field of a quarter-infinite crack in a half-space. Thus the eigenvalues in the present problem are obtained by computing the eigenvalues of a quarter infinite crack according to the procedure in the previous section(for detail see Ref. 5-6). The eigenvalues and its corresponding eigenfunctions of a quarter infinite crack depend upon Poisson's ratio, ν. Therefore varying Poisson's ratio, the eigenvalues are computed and tabulated in Table 1. From this table, verified is the complementary relation $\lambda + \lambda^c = -1$: that is, eigenvalue λ appears as a complementary pair. The stress singularities are defined as the eigenvalues in the range of $0 < \mathrm{Re}(\lambda) < 1$, that comes from the requirements that the strain energy and the displacements at the origin are bounded. The stress singularities are compared with the stress singularities computed by other studies in Fig. 5.

Table 1 Complementary pairs of eigenvalues for the symmetric deformation($\lambda + \lambda^c = -1$)

ν=0.0	ν=1.5	ν=3.0	ν=4.0
-2.0052	-2.0046	-2.0040	-2.0035
-2.0001	-2.0002	-2.0003	-2.0006
-1.5010	-2.5173	-1.5471	-1.5863
-1.0013	-1.0011	-1.0010	-1.0013
-1.0003	-1.0003	-1.0002	-1.0002
0.0003	0.0003	0.0002	0.0002
0.0013	0.0011	0.0010	0.0013
0.5010	0.5173	0.5471	0.5863
1.0001	1.0002	1.0003	1.0006
1.0052	1.0046	1.0040	1.0035

By using the two-state M-integral, i.e., Eq. (13) and the Eq. (15), the intensities corresponding to the stress singularities are computed varying Poisson's ratio in Table 2. Using the computed intensities, we plot the stresses obtained from the asymptotic solutions and the stresses obtained from the finite element results in the direction $(\theta, \phi) = (\pi/2, \pi)$ versus distance from the crack corner in Fig. 6. The asymptotic solutions accurately describe the elastic stress fields close to the crack corner. However they do not describe well on the far field where the solutions are perturbed by not only the nonsingular terms but also the far-field geometry and the boundary conditions. Thus we can determine the dominant region of the stress singularity by comparing the asymptotic solutions and the finite element results.

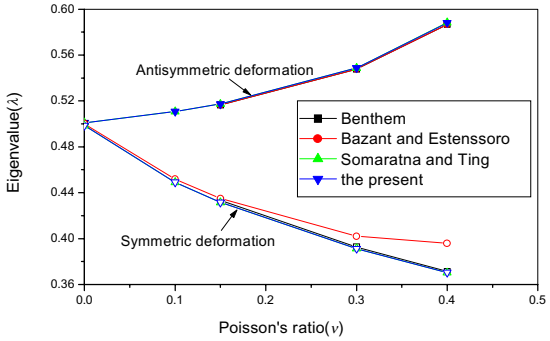

Fig. 5 The stress singularities of a quarter infinite crack

Table 2 Intensities varying Poisson's ratio

Poisson's ratio	Intensity β_s
0.0	21.640
0.15	22.162
0.3	24.845
0.4	25.480

Conclusions

We proposed a methodology to compute the stress intensities at three dimensional crack corners using the two-state M-integral via a regular displacement based FEM without resort to special techniques.

The existence of the complementary eigenvalues in the M-integral sense, which comprises the key to success of the present computational scheme together with the path independence of the two-state M-integral, has been verified for three dimensional crack corners.

Acknowledgments

This work was supported by Korea Science and Engineering Foundation.

References

1. Bazant, Z. P. and Estenssoro, L. F., "Surface singularity and crack propagation," *Int. Int. J. Solids Structures*, Vol. 15, (1979), pp. 405-426.
2. Benthem, J. P, "State of stress at the vertex of a quarter-infinite crack in a half-space," *Int. J. Solids Structures*, Vol. 13, .(1977), pp. 479-492.
3. Benthem, J. P., "The quarter-infinite crack in a half-space; alternative and additional solutions," *Int. J. Solids Structures*, Vol. 16, (1980), pp. 119-130.
4. Somaratna, N. and Ting, T. C. T., "Three dimensional stress singularities at conical notches and inclusions in

transversely isotropic materials," *ASME J. Appl. Mech.*, Vol. 53, (1986a), pp. 89-96.

5. Somaratna, N. and Ting, T. C. T., "Three-dimensional stress singularities in anisotropic materials and composites," *Int. J. Engng. Sci.*, Vol. 24, No. 7(1986b), pp. 1115-1134.
6. Ghahremani, F., 'A numerical variational method for extracting 3D singularities,' *Int. J. Solids Structures*, Vol. 27, No. 11(1991), pp. 1371-1386.
7. Ghahremani, F. and Shih, C. F., 'Corner singularities of three-dimensional planar interface cracks,' *ASME J. Appl. Mech.*, Vol. 59, (1992), pp. 61-68.
8. Picu, C. R. and Gupta, V., 'Three-dimensional stress singularities at the tip of a grain tiple junction line intersecting the free surface,' *J. Mech. Phys. Solids*, Vol. 45, No. 9(1997), pp. 1495-1520.
9. Koguchi, H., "Stress singularity analysis in three-dimensional bonded structure," *Int. J. Solids Structures*, Vol. 34, No. 4(1997), pp. 461-480.
10. Glushkov, E., Glushkova, N. and Lapina, O., '3-D elastic stress singularity at polyhedral corner points,' *Int. J. Solids Structures*, Vol. 36, (1999), pp. 1105-1128.
11. Koguchi, H. and Muramot, T., "The order of stress singularity near the vertex in three dimensional joints," *Int. J. Solids Struct.*, Vol. 37, (2000), pp. 4737-4762.
12. Labossiere, P. E. W. and Dunn, M. L., "Fracture initiation at three-dimensional bimaterial interface corners," *J. Mech. Phys. Solids*, Vol. 49, (2001), pp. 609-634.
13. Nakamura, T. and Parks, M. D., "Antisymmetrical 3-D stress field near the carck front of a thin elastic plate," *Int. J. Solids Struct.*, Vol. 25, (1989) 12, pp. 1411-1426.
14. Chen, F. H. K. and Shield, R. T, "Conservation laws in elasticity of the J-integral type," *J. Appl. Math. & Physics ZAMP*, Vol. 28, .(1977), pp. 1-22.
15. Im, S. and Kim, K. S., 'Application of the two-state M-integral for computing an intensity of singular near-tip field for a generic composite wedge, *J. Mech. Phys. Solids*, Vol. 48, (2000), pp. 129-151.
16. Lee, Y., Goo, N. S. and Im, S., "Application of two-state M-integral for analysis of adhesive lap joints," *Int. J. Num. Methods Engng.*, Vol. 52, (2001), pp.903-920.
17. Im S. and Lee Y., "Complementarity of the Eigenvalues in the three dimensional wedges," *Asian-Australasian Conference of Composite Materials(ACCM-2000)*, (2000) pp. 555-570, Kyungju, Korea.
18. Knowles, J. K. and Sternberg, E., "On a class of conservation laws in a linearized and finite elatostatics," *Arch. Rat. Mech. Anal.*, Vol. 44, (1978), pp.187-211.
19. Leguillon, D. and Sanchez-Palencia, E., *Computation of singular solutions in elliptic problems and elasticity*, Masson, (Paris, 1987).

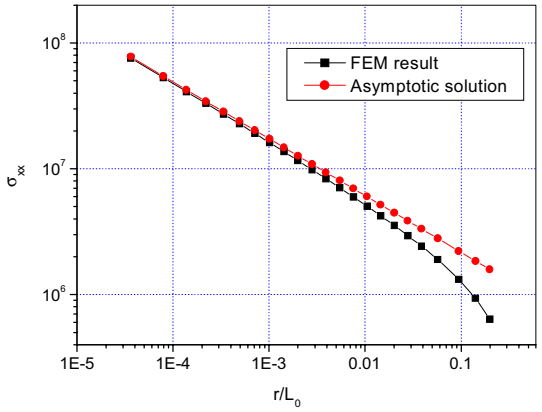

(a)

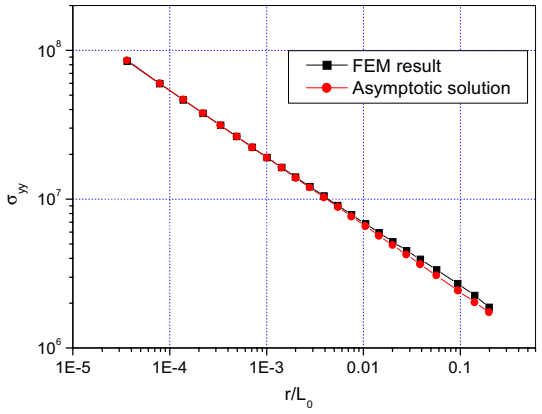

(b)

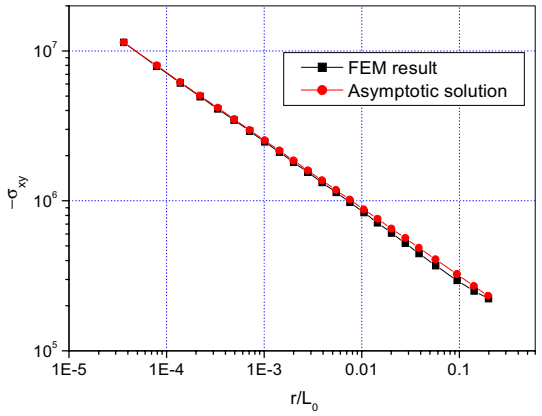

(c)

Fig. 6 Comparison of the finite element solutions, the singular solution of three dimensional crack corners(ν=0.3); (a) σ_{xx}, (b) σ_{yy}, (c) $-\sigma_{xy}$.